JGR Solid Earth

RESEARCH ARTICLE
10.1029/2022JB025050

Beamforming of Rayleigh and Love Waves in the Course of Atlantic Cyclones

J. D. Pelaez Quiñones[1,2], D. Becker[1,3], and C. Hadziioannou[1]

[1]Institute of Geophysics, University of Hamburg, Hamburg, Germany, [2]Now at Université Côte d'Azur, CNRS, Observatoire de la Côte d'Azur, IRD, Géoazur, Sophia Antipolis, Valbonne, France, [3]Now at GFZ German Research Centre for Geosciences, Potsdam, Germany

Key Points:

- Primary and secondary microseismic Love and Rayleigh waves excited by Atlantic cyclones were detected via onshore polarization beamforming
- We observed microseisms related to cyclones as they pass over the northwestern Atlantic margin off Newfoundland
- Some microseisms have constant direction of arrival, others are azimuthally progressive and reflect the advance of the cyclone

Supporting Information:

Supporting Information may be found in the online version of this article.

Correspondence to:

J. D. Pelaez Quiñones,
julian.david.pelaez-quinones@uni-hamburg.de;
pelaez@geoazur.unice.fr

Citation:

Pelaez Quiñones, J. D., Becker, D., & Hadziioannou, C. (2023). Beamforming of Rayleigh and Love waves in the course of Atlantic cyclones. *Journal of Geophysical Research: Solid Earth*, *128*, e2022JB025050. https://doi.org/10.1029/2022JB025050

Received 30 JUN 2022
Accepted 11 FEB 2023

Author Contributions:

Conceptualization: J. D. Pelaez Quiñones, D. Becker, C. Hadziioannou
Data curation: J. D. Pelaez Quiñones
Formal analysis: J. D. Pelaez Quiñones
Funding acquisition: C. Hadziioannou
Investigation: J. D. Pelaez Quiñones, D. Becker
Methodology: J. D. Pelaez Quiñones, D. Becker, C. Hadziioannou
Project Administration: J. D. Pelaez Quiñones, D. Becker, C. Hadziioannou

Abstract The main sources of the ambient seismic wavefield in the microseismic frequency band (peaking in the ~0.04–0.5 Hz range) are earth's oceans, namely the wind-driven surface gravity waves (SGW) that couple oscillations into the seafloor and the upper crust underneath. Cyclones (e.g., hurricanes, typhoons) and other atmospheric storms are efficient generators of high ocean waves that in turn generate distinct microseismic signatures. In this study, we perform a polarization (i.e., three-component) beamforming analysis of microseismic (0.05–0.16 Hz) retrograde Rayleigh and Love waves during major Atlantic hurricanes using a virtual array of seismometers in Eastern Canada. Oceanic hindcasts and meteorological data are used for comparison. No continuous generation of microseism along the hurricane track is observed but rather an intermittent signal generation. Both seismic surface wave types show clear cyclone-related microseismic signatures that are consistent with a colocated generation at near-coastal or shallow regions, however the Love wavefield is comparatively less coherent. We identify two different kinds of intermittent signals: (a) azimuthally progressive signals that originate with a nearly constant spatial lag pointing toward the trail of the hurricanes and (b) azimuthally steady signals remaining nearly constant in direction of arrival even days after the hurricane significantly changed its azimuth. This high complexity highlights the need for further studies to unravel the interplay between site-dependent geophysical parameters, SGW forcing at depth and microseismic wavefield radiation and propagation, as well as the potential use of cyclone microseisms as passive natural sources.

Plain Language Summary Ocean waves are responsible for the generation of microseisms, faint ground vibrations with complex characteristics and which comprise a major portion of the background seismic noise of the earth. In this study, we implement an onshore seismic detection method to study microseisms generated by cyclones in the North Atlantic ocean (hurricanes), as these are known to be major generators of large ocean waves. We observed that cyclones only seem to generate detectable microseisms as they move over certain regions in the ocean, namely near coastal or shallow water regions. The direction of arrival of these microseisms is sometimes constant, at other times it shifts azimuth along with the hurricanes. Understanding the relationship between ocean waves and cyclone-related microseisms is an important step for the potential use of these vibrations to study the earth, ocean and atmosphere.

1. Introduction

Atmospheric phenomena and ocean waves have long been known to be intimately related, and the imprint of the latter in seismological records has been persistently pointed out (e.g., Gutenberg, 1936; Kibblewhite & Wu, 1996; Longuet-Higgins, 1950; Nishida, 2017). Water column pressure fluctuations induced by wind-driven surface gravity waves (SGW) and swells couple into the seafloor and produce elastic waves in the solid earth, so called *ocean microseisms*. Evidence suggests that cyclones have become increasingly stronger worldwide since the last four decades owing to global warming (Kossin et al., 2020). Additionally, their latitude of formation and maximum magnitude is shifting polewards (Kossin et al., 2014), their built-up rate has sped-up (Emanuel, 2017b) and their associated rainfall volume has increased (Emanuel, 2017a). The societal relevance of cyclones has thus grown accordingly at the same time that other effects of climate change such as sea-level rise make the scenario more concerning. While cyclones have been traditionally the subject of study for meteorologists and oceanographers, understanding their dynamics and what to expect from them in the near future is also of great interest for other fields. Concretely, the analysis of microseisms has the potential to contribute to the understanding of the mechanical coupling between the atmosphere, ocean and solid earth.

Resources: J. D. Pelaez Quiñones, D. Becker, C. Hadziioannou
Software: J. D. Pelaez Quiñones
Supervision: D. Becker, C. Hadziioannou
Validation: J. D. Pelaez Quiñones, D. Becker, C. Hadziioannou
Visualization: J. D. Pelaez Quiñones, D. Becker
Writing – original draft: J. D. Pelaez Quiñones, D. Becker
Writing – review & editing: J. D. Pelaez Quiñones, D. Becker, C. Hadziioannou

Previous studies have reported ocean microseisms related to storms and hurricanes (both sub-types of cyclones) (e.g., Gilmore, 1947; Gutenberg, 1958; Haubrich et al., 1963; Sutton & Barstow, 1996). Ocean microseisms are generally divided into primary (PM), having the same frequency as the causative SGW and being generated often close to the shore, and secondary microseisms (SM), with twice the frequency of the forcing SGW. Teleseismic observations of both, deep- and shallow-water microseisms exist (e.g., Beucler et al., 2015; Kedar et al., 2008; Landès et al., 2010; Traer et al., 2012; Ying et al., 2014) and the theoretical understanding of the ocean-seafloor-subsurface coupling has been developed since early works (e.g., Longuet-Higgins, 1950, 1953) up to more recent advances (e.g., Ardhuin et al., 2011; Retailleau & Gualtieri, 2021). However, a detailed knowledge on the localization of the cyclone-related microseismic sources, as well as their shape, spectral characteristics and their exact relation with the physical properties of the generating cyclones is still in development. The generation mechanism behind Love waves has been a particular object of debate: these are proposed to result from vertical water pressure interactions with sloping/irregular bathymetry (Fukao et al., 2010; Saito, 2010), horizontal tractions due to ocean wave movement (Ardhuin et al., 2015; Juretzek & Hadziioannou, 2017), or to a minor extent on wave conversions and multiple scattering (Ziane & Hadziioannou, 2019).

The beamforming approach to study cyclones can be traced back to the early studies by Cessaro and Chan (1989), who at the time used single-component frequency-wavenumber ($f - k$) beamforming to locate surface wave PM sources during the passage of two cyclones near the Pacific and Atlantic coasts of Canada with two land-based arrays, one in Alaska and the other inland Canada. The authors concluded that the analyzed signals (allegedly Rayleigh waves) had enough stability over one-hour windows to be useful for triangulation and that most energy came from near-shore processes that could be linked to the storms. No continuous tracking was sought by the authors and only a broad source area was triangulated. Later, Cessaro (1994) extended the study of Rayleigh waves into the SM band and included NORSAR as a third array in an attempt for continuous tracking. The author found that backazimuths do not follow the storm track directly. SM results are described as more stochastic, sporadically meandering around the synoptic region of peak SGW activity, while PM sources appeared more stable and localized, lying over specific near-shore regions in the Labrador sea and off the coast of western North America. Overall, the results of both studies had low space-time resolution but demonstrated that the seismic array detection of cyclones is possible.

Later microseismic beamforming studies focused on regional ambient microseisms using pre-existing seismic arrays to resolve the dominant generation areas during longer time intervals (e.g., Essen et al., 2003; Euler et al., 2014; Friedrich et al., 1998; Juretzek & Hadziioannou, 2017). Single-cyclone tracking was not the main aim of these studies but rather to define the dominant microseism spatial distribution over a given timespan. Friedrich et al. (1998) for example, used polarization beamforming at Graefenberg and NORSAR arrays to define a dominant source at the north-Norwegian coast. The Love/Rayleigh energy ratios in their study were found to be much higher for PM than for SM ambient noise, indicating possible differences in source mechanisms. Ward Neale et al. (2018) used the P-wave beamformer output of multiple arrays to produce a combined output image overlaid on a geographical grid. According to the authors, their procedure sharpened and improved the coverage of the image in comparison to a single array. However, mixed results were found in terms of storm location, as some arrays failed to locate the storms under study. A similar problem was encountered by Wang et al. (2021), who discuss that "(surface wave microseismic) sources could be suppressed if they are below the detectability of one of the arrays." Both studies quote the large array-storm inter-distances as a relevant cause for this. Other studies using seismic arrays have focused on the analysis of particular cyclones and their microseisms in detail (e.g., Barruol et al., 2016; X. Chen et al., 2015; Gerstoft et al., 2006; Lin et al., 2017; Sufri et al., 2014; Tanimoto & Valovcin, 2015).

The concrete goal of our study is to implement the polarization (3-component) beamforming method to analyze and compare the seismic surface wavefield (Rayleigh and Love) in the microseismic frequency band (~0.05–0.16 Hz) during a few major north Atlantic cyclones (hurricanes), as this is one of the regions in the world with the highest cyclone activity every year. In contrast to station configurations deliberately installed for array analysis (e.g., NORSAR, Graefenberg) we here utilize a virtual array consisting of onshore seismometer stations of the World-Wide Standardized Seismograph Network originally deployed for routine earthquake monitoring near the western North Atlantic coast, close to the ocean strip crossed by the cyclones under study. The generation regions of the observed microseisms is of particular importance, as some debate still exists on the topic. In this study, we also compare the spatio-temporal characteristics of the Rayleigh and Love wavefields, as several studies tend to consider only one of these wave types, or alternatively body waves (e.g., Gerstoft et al., 2008). We study the PM

and SM wavefields in detail seeking to relate them to the progression of the hurricane track, link their generation to specific regions and potentially to meteorological and oceanographic characteristics. In contrast to earlier studies (Cessaro, 1994; Cessaro & Chan, 1989), the polarization beamforming processing implemented here as well as the use of modern seismic records allowed for the introduction of Love phase analysis and improved the achievable space-time resolution. In addition, the hindcasts and cyclone meteorological data at the high resolution and with the computational and model improvements currently available for our analysis were not available for the earlier studies. Generally speaking, we intend to contribute to the understanding of the complex relationship between atmospheric and seismic phenomena by gathering information on the ambient seismic wavefield during major hurricanes.

In the following sections, a short review on cyclones and microseisms, the data and the study region are presented. Then, we outline the beamforming method and show results for selected hurricanes including a detailed discussion. Finally, we summarize the most relevant observations and some of their implications.

2. Cyclones and Microseisms

Cyclones are low-pressure center convective weather systems with well-defined structures and life-cycles that develop mostly over the ocean in the tropics and mid-latitudes, where warm waters are available. Depending on their maximum 1-min sustained windspeeds, tropical cyclones (those that form almost exclusively in tropical regions) are referred to (in increasing order) as *tropical depressions*, *tropical storms*, *typhoons* (in the western pacific ocean) or *hurricanes* (in the eastern pacific and Atlantic ocean) (Wallace & Hobbs, 2006). When tropical cyclones move into medium or high latitude regions, these are denoted as: subtropical and extratropical, respectively. Cyclones are mostly clustered in the *tropical cyclone season*, during which the strongest ones occur. The Atlantic hurricane season peaks typically during the Northern summer (between June and October). The center (eye) of cyclones usually has a radius between 10 and 60 km, while the entire systems have ROCIs (radius of the outermost closed isobar, a measure to define the radius of a cyclone up to its outermost wind circulation region) from about 200 km up to 1,000 km. Their paths are often erratic, controlled by Coriolis effect and high-level winds but covering in average recurrent geographical corridors, translating roughly westward from the tropical Atlantic region where they form between the western tip of Africa and Middle America at about 2–10 m/s as they widen and intensify, and then shifting polewards to diffuse and weaken by cold waters or land along their path, to finally reach translational speeds of up to 25 m/s (Ochi, 2003). Cyclones are traditionally monitored in real-time and studied via satellite images, on- and offshore meteorological/oceanographic point measurements and hind-/forecast models.

Wind blowing over the sea surface is known to be the major cause for ocean surface gravity waves (SGW) at frequencies $\gtrsim$0.01 Hz (Knauss, 1997) and their waveheights are proportional to the speed, timespan and fetch of the wind (Young, 1998). The strong winds of cyclones force the water surface to develop wind waves that later evolve into long-period swells as they radiate away more or less radially. The directional SGW spectrum of cyclones is rather complex, especially during landfall (S. Chen & Curcic, 2015). In the Northern hemisphere, the highest SGW tend to occur at the frontal sector (i.e., front left and right quadrants) of the cyclone (in traveling direction), near the area where windspeeds are highest (Esquivel-Trava et al., 2015; Wallace & Hobbs, 2006). Because winds are a superposition of the forward motion of the storm and the circulating air, their intensity is the highest in the right (left) quadrants in the Northern (Southern) hemisphere. Farther away from the eye the SGW spectra become multimodal, consisting of a superposition of local wind-sea and swells (low frequency SGW after propagating large distances from their sources). Young (2006) explains that wave period is proportional to maximum wind speed (and thus wave propagation speed) and that swells originating near the intense wind crescent at an earlier point in the track dominate in all its quadrants except for the right-rear. Hu and Chen (2011) argue that the dominant wave direction in the front quadrants radiate out from the right of the eye, while in the rear are mostly locally generated, except for the rear left quadrant where outward radiation is also evident.

The high amplitude SGW resulting from cyclones are known to generate both PM and SM. SM is commonly cited to be more energetic and generated by non-linear wave-wave interactions between SGW of nearly the same frequencies traveling at quasi-opposite directions, which would result in standing SGW with amplitudes proportional to the product of the original waves, doubled frequencies (DF) and hydroacoustic waves that reach the ocean bottom traveling downwards nearly unattenuated (Hasselmann, 1963; Kibblewhite & Wu, 1996; Longuet-Higgins, 1950). Alternatively, it has been proposed that SM are caused directly by water column

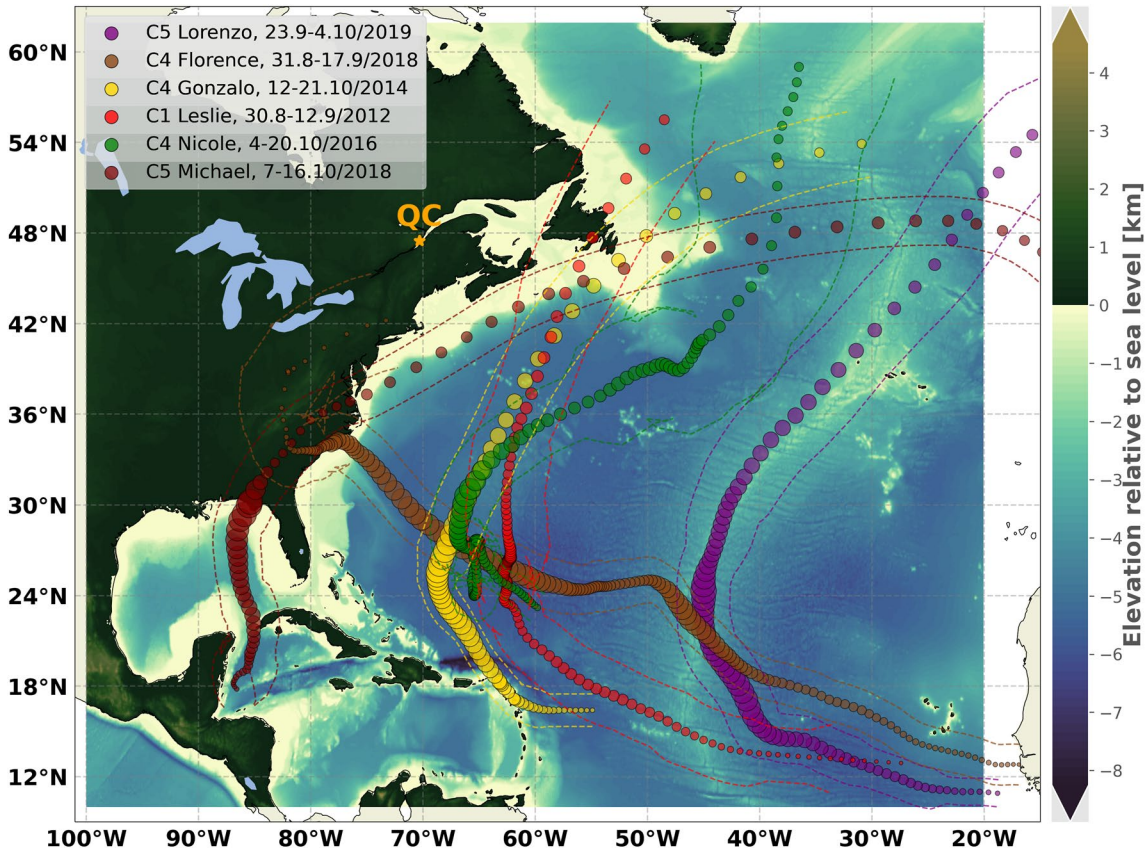

Figure 1. Atlantic hurricanes considered in this study. Categories (C1-C5) correspond to Saffir-Simpson scale. Dots mark the locations of the *eye* of the hurricane at 3 hr-time steps. Their radius is proportional to the maximum sustained wind speeds (see Figure 5 for absolute values), while the dashed lines mark the width (ROCI) of the system. The orange star marks the location of the QC array. Hurricane track data obtained from IBTrACS (Knapp, Kruk, et al., 2010).

pressure propagation under Bernoulli's principle and via cylindrical wave radiation around the center of cyclones (Bowen et al., 2003). SM have frequencies above ~0.08 Hz in the open ocean and up to ~1 Hz locally at marginal seas (Becker et al., 2020), but tend to generate the strongest ocean microseisms in the ~0.1–0.2 Hz band. PM are thought to arise from ocean wave shoaling and SGW-seabed interactions over relatively shallow waters (Ebeling, 2012; Nishida, 2017). The typical frequencies of the latter in the ocean are in the range ~0.05–0.1 Hz (10–20 s-periods).

3. Data

3.1. Selected Hurricanes

A total of six cyclones were selected for our study to compare their microseismic signatures: C1 Leslie (2012); C4 Gonzalo (2014); C4 Nicole (2016); C4 Florence (2018); C5 Michael (2018); and C5 Lorenzo (2019). These were mostly strong North Atlantic atmospheric events lasting about a couple of weeks at most, that are accordingly expected to generate strong microseismic signals. Figure 1 summarizes their trajectories and dates of activity. The categories, geographical paths, ocean depth ranges and inter-distances to the array center were chosen to be diverse to compare their distinct characteristics and detection capability. As every major cyclone strengthens gradually, analyzing the strongest ones provides the advantage of including stages of lower categories as well as higher ones. It additionally balances out potential attenuation issues at the far field, as stronger microseisms are expected for stronger SGW forcing. Relatively simple and long trajectories were preferred to increase the probability of tracking. Some of the tracks share relatively similar Northwards routes near the northwestern Atlantic ocean margin that potentially allow for the identification of common microseismic patterns. Ocean state hindcasts as well as hurricane best-track data on the study region during the passage of these hurricanes was retrieved for comparison with the seismic approach results.

3.2. Seismic Data

The beamforming methodology requires the joint analysis of seismic stations conforming an array. Land stations forming an optimal array close to the path of the selected cyclones (at the northeastern coast of North America) were selected. The array aperture (A) was required to be no less than about half the maximum wavelength of the microseismic surface waves expected (having periods in the range ~5–25 s and typical speeds of 2.7–4.5 km/s): $A \geq \lambda_{max}/2 \approx 25/2$ s × 4 km/s ≈ 50 km for the fastest Love waves in the crust. This ensures enough resolution power throughout the full frequency range of interest. To avoid spatial aliasing at the shortest wavelengths, we sought that inter-station distances remained below $\sim\lambda_{min}$ (~16 km for the slowest signals at 0.16 Hz), although this is not always fulfilled due to the limited number of densely clustered FDSN broadband stations available (groups of 6–10 at most). The geometry was also expected to have a diverse distribution of inter-station distances and a non-regular geometry to suppress side lobes in the transfer function (i.e., the array response function—ARF), which describes the performance of the array (Nakata et al., 2019).

Potential virtual arrays were found at a few locations around the Atlantic ocean (e.g., Quebec, Oklahoma, Virginia, Guadeloupe, Pyrenees) but sizes were usually too large for surface wave microseismic analysis, having typical apertures of more than 150 km and inter-station distances of more than about 30 km. This happens because most stations in the global network were not intended to be used for array analysis but rather for earthquake observation and deep tomography in wide, global networks. Station spacing of the USArray was generally too large to build an optimal array therein. Additional limitations included: lack of data available, insufficient number of stations (less than 5) and inadequate geometries (poor ARFs). Some pre-existing arrays that border the study region were designed for higher frequencies (e.g., GERES, SPITS) and their apertures are thus too small, while others were too far apart from the Atlantic hurricane path zone (e.g., Gräfenberg, NORSAR, YKA).

A virtual array lying in a flat and seismically quiet area that we named "QC" near Saint Lawrence river in Quebec, Canada was arranged by selecting broadband stations of the Canadian National Seismograph Network (CN). This array fulfilled the criteria for our study due to its proximity to the western Atlantic coast and ideal mean station spacing (about 20 km), resulting in an aperture of ~69–104 km (depending on missing data) that is optimal for the frequency range under analysis, while also covering more than five stations for an adequate signal-to-noise ratio (SNR). Figure 2 shows its geometry and the ARF, that is, its beamforming transfer function for two different frequencies. The ARF at 0.06 Hz (in the PM range) has a broad and prominent main lobe and a few weak side lobes, while that for 0.12 Hz (in the SM range) is more affected by numerous side lobes while having a sharper central maximum. The latter is due to the mean inter-station distances, which lead to a minor degree of spatial aliasing of the shortest wavelengths without implicating our results. See Text S1 in Supporting Information S1 for an additional description of the data.

A single array limits our observations to the azimuthal plane and increases the far-field attenuation effect given the lack of distributed measurements. However, the joint time-lapse beamforming analysis with an optimal array, the hurricane best-tracks and the ocean hindcast data of several hurricanes compensates these limitation to some degree, while contributing significantly to the interpretation and comparison of the observed signals. Section 6.5 outlines a complementary discussion on the practical limitations of the array methodology.

3.3. Hindcast Data

In order to compare the microseismic signatures with the ongoing distribution of ocean state anomalies, hindcasts from a global oceanic model were used (see further details in Text S2 of Supporting Information S1). The variables related to microseisms chosen for this study are:

- **Waveheight**: significant ocean wave height in meters. Represents the mean trough-to-crest amplitude of the highest waves in a region and is treated here as four times the standard deviation of the ocean surface elevation. It is expected to be proportional to the amplitudes of PM signals and partially to those of SM.
- **p2l (*or* S_{DF}):** Power spectral density (frequency spectrum) of the equivalent second-order SGW-induced pressure fluctuation near the water surface (S_{DF} in Equation S1 in Supporting Information S1), which is a proxy for the strength of the nonlinear interaction of colliding SGW in opposite directions, and indirectly a proxy for the intensity of the associated SM signal with double frequency (DF) relative to the causative SGW (Stutzmann et al., 2012). This includes microseisms due to interaction of storm wind waves. The results are given in $\log_{10}(Pa^2m^2s \times 10^{12})$. It empirically takes coastal reflections into account based on bathymetry and

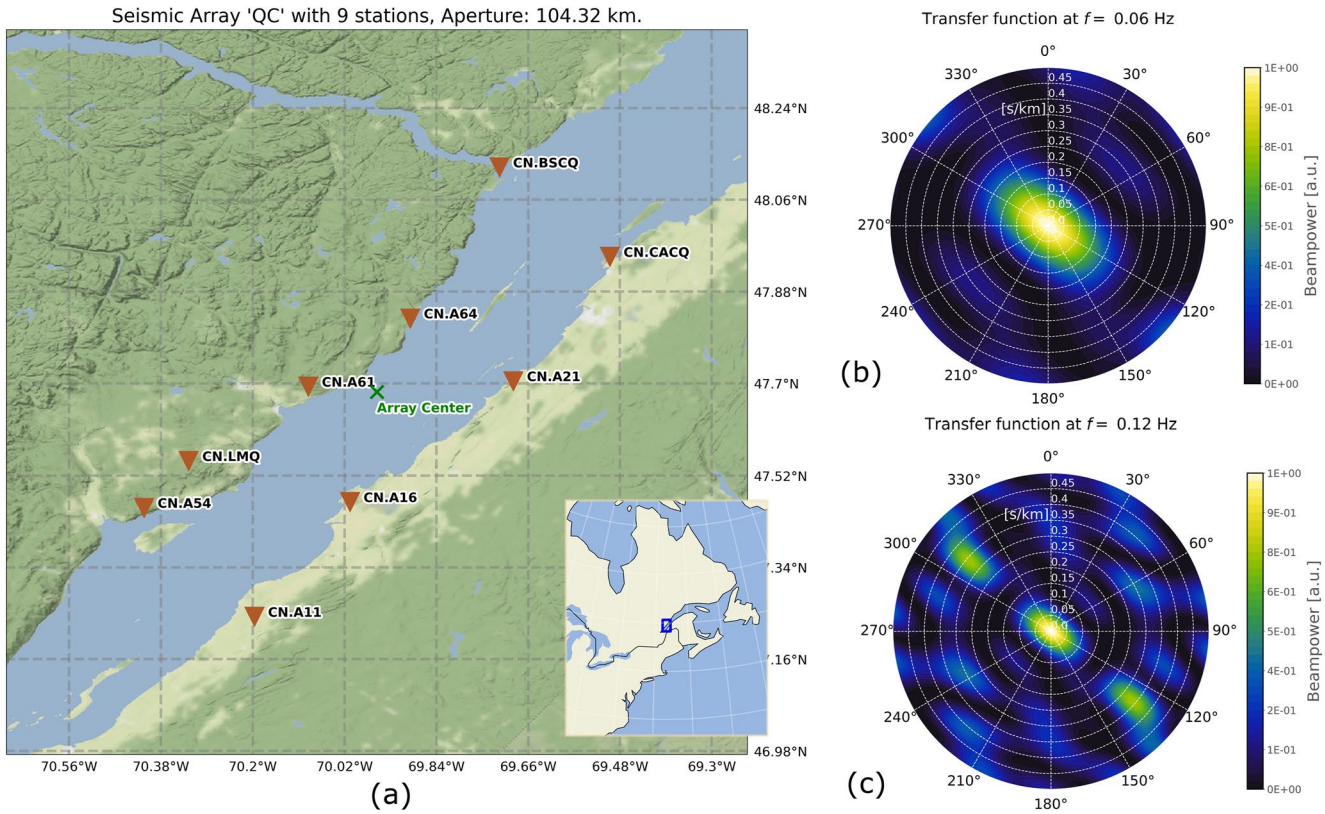

Figure 2. (a) QC array geometry with inverted triangles indicating the seismic stations. The corresponding transfer functions (ARFs) are indicated for (b) 0.06 Hz and (c) 0.12 Hz. Stations CN.CACQ and CN.BSCQ are not taken into account for these ARFs, but doing so improves their quality (see Section 3.2 for explanation).

coastal shape but other site effects at the source region are not considered (Gualtieri et al., 2021). To correct for this, the bathymetry amplification factors for land-measured microseismic Rayleigh waves for typical crustal parameters as proposed by Tanimoto (2013) are considered (See Text S3 in Supporting Information S1 for a detailed description of this variable as here implemented).

4. Methods and Data Processing

4.1. Polarization Beamforming

After pre-processing of the raw seismic data (see Text S4 in Supporting Information S1 for details), polarization beamforming that is, three-component beamforming (Esmersoy et al., 1985; Löer et al., 2018; Nakata et al., 2019) was implemented to determine the Love and Rayleigh wave directional contributions in the microseismic wavefield measured at our virtual network. The goal of beamforming is to separate the coherent portion of the recorded wavefield from the stochastic one. This is done by generating outputs (*beams*) with the largest possible SNR, which (in time domain) are geometrical propagation-dependent stacks of lagged input traces or equivalently (in frequency domain) the weighted linear superposition of Fourier transforms of the cross-correlation between every pair of recordings, as here implemented. If coherent and prominent signals exist, the suitable set of weights among a space of possible combinations increases the output power, that is, the *beampower* (BP), which in turn remains comparatively low if uncorrelated noise dominates. BP can be expressed in the frequency (f) domain as (Nakata et al., 2019):

$$BP(f) = \frac{1}{L^2 M^2}\mathbf{w}^H \mathbf{X}(f)\mathbf{X}^H(f)\mathbf{w} = \frac{1}{M^2}\mathbf{w}^H \mathbf{C}(f)\mathbf{w}, \quad (1)$$

where H denotes a conjugate transpose, L is the number of samples, M the number of sensors and $\mathbf{X}(f)$ contains the Fourier transform of each recording. The entries in $\mathbf{w}$ are the so-called weights that maximize BP depending on the assumed wave type (e.g., polarization state and wavelength) as well as the array geometry. The term

C(f) is known as the cross spectral density matrix and can be thought of as the kernel of beamforming, having information on the phase-delay relations between every pair of spectra from any two sensors, namely the Fourier transform of the auto/cross-correlation between every pair of stations. For details on the implementation of beamforming see Text S5 in Supporting Information S1.

BP can be regarded as a measure of the relative coherency and implicitly the amplitude of the signal traveling through an array. Coherency refers in our context to the degree of agreement/predictability of a signal under a particular propagation model, or alternatively, as the degree of certainty to relate the signal to a unique source acting at a defined location and over a given time span. In the approach used here, a single, plane wavefront will produce a high BP value while several interfering sources or bent wavefronts would result in lower BP values.

We investigated two polarization states of the microseismic wavefield: elliptic retrograde and transverse, representing retrograde Rayleigh waves and Love waves, respectively. We set the slowness range to 0.22–0.37 s/km in order to include only surface waves and exclude most of the body wave energy or other undesired phases. The beamforming analysis window length (T_{BF}) was set to 300 s with a 50% overlap of consecutive windows, and the covariance matrix was averaged over 24 time windows, so that the output snapshots have a 1-hr resolution, unless otherwise specified. Performance tests to detect earthquakes of magnitude as low as 5.0 were successful. However a typical backazimuth (β) deviation of $\pm 5°$ was observed, so that this can be considered an implicit uncertainty of our estimates.

5. Results

In the following, the polarization beamforming results for two hurricanes (C1 Leslie in 2012 and the last four days of C4 Gonzalo in 2014, see Figure 1) at PM and SM frequencies are presented first to analyze their microseismic signatures in detail, as these hurricanes showed remarkable features. Thereafter, results for all the hurricanes considered are summarized.

5.1. Leslie and Gonzalo—Primary Microseisms

Z-component spectrograms recorded at a station CN.LMQ of the QC array during hurricanes Leslie (Figure 3a) and Gonzalo (Figure 3b) depict microseismic signals with variable frequency content lasting from several hours to several days, with superposed sporadic spikes related to the imperfect removal of earthquakes and local noise. A lobe of relatively continuous PM energy below 0.1 Hz is observed during the last stages of Leslie (indicated by a black circle). The double-frequency (DF) phenomenon is particularly clear during Gonzalo, as the low-frequency PM features repeat themselves with stronger amplitudes and twice the frequencies in the SM range between the 17-20th of October. The linear trends during the dissipation stage (black segments) approximate the dispersion of prominent microseismic arrivals, which are typical of storms. Based on the short-wave (deep water) linear SGW group velocity dispersion relation ($U_g = g/4\pi f$) as in Bromirski and Duennebier (2002), a distance (Δx) from the SGW source (a region presumably within the ROCI of the storm) to the microseismic source region can be roughly estimated from the slopes of these linear trends ($\Delta f/\Delta t$) by using:

$$\Delta x = \frac{g}{4\pi}\frac{\Delta t}{\Delta f} \tag{2}$$

where g is the acceleration of gravity at sea level and t represents time. This yields an estimated distance in the range 600–1,000 km, which is somewhat above the average radius of these hurricanes during dissipation stage (~450 km). This is just a rough estimate, as hurricanes are not stationary SGW sources and the spectral slopes are thus diffuse to some extent. Furthermore the hurricane and the microseismic source areas are both generally irregularly shaped and Equation 2 is only valid for short waves. However, since the observed microseismic pulses have marked linear slopes, the relationship is preserved to some extent.

Figures 3c–3f show the maximum BP values in the time-backazimuth (t, β) space picked over the slowness range for each time and azimuth step. The BP was pre-averaged at each slowness step in the PM frequency band (0.05–0.09 Hz). The features in the spectrograms partially match those in the beamforming results for both Rayleigh (Figures 3c and 3d) and Love (Figures 3e and 3f) waves during Leslie (left column) and Gonzalo (right column). Colored dots depict the true bearing toward the center of the investigated hurricane and the red dashed

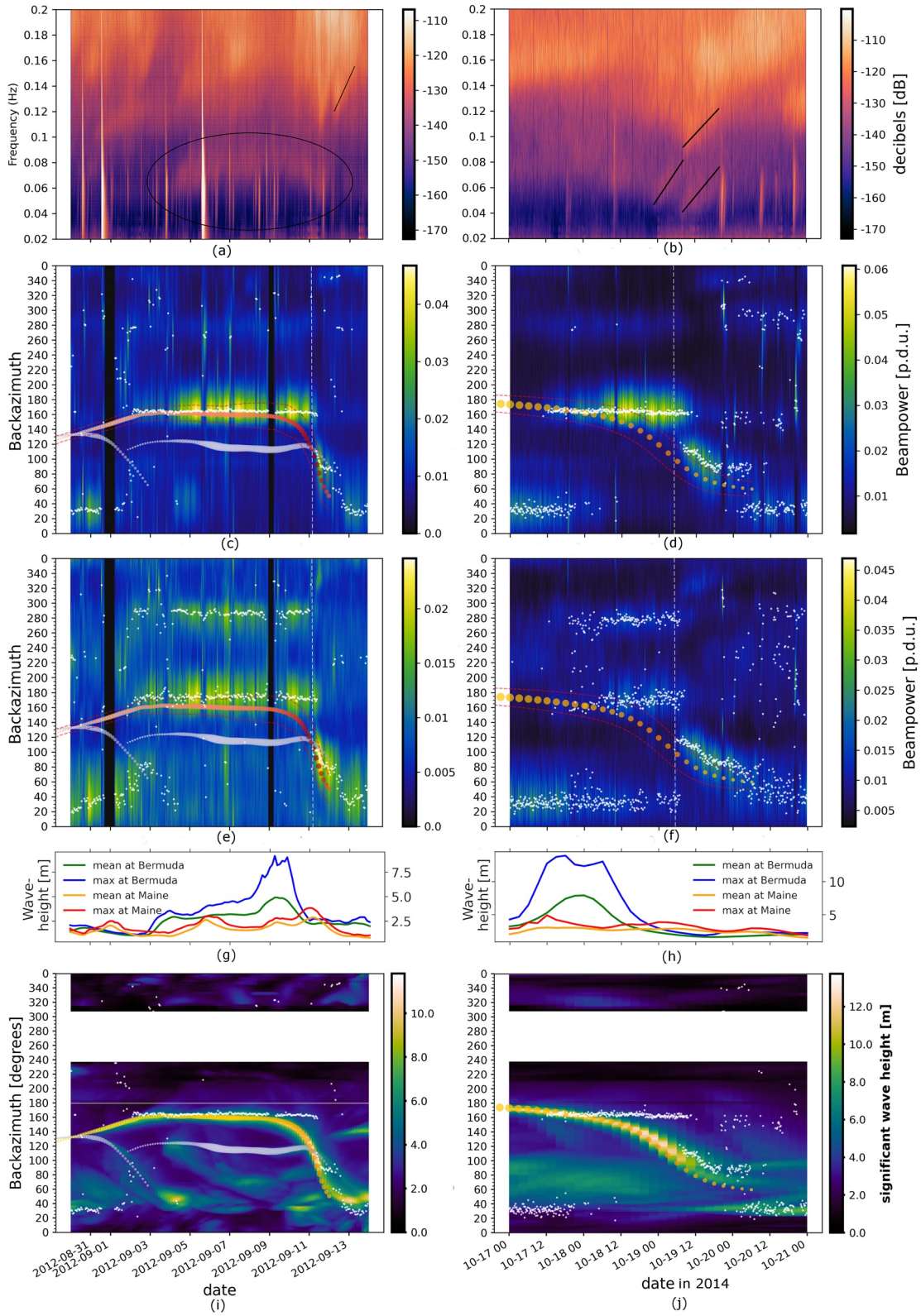

Figure 3.

lines depict its outermost winds from the perspective of the QC array, respectively. White dots represents the global and most prominent local BP maxima for each time step.

Based on Figure 3c–3f, a set of observations can be pointed out: (a) two types of BP signals stand out that can be related in time and space to the tracks of the main hurricanes: azimuthally steady (i.e., static, displaying constant backazimuths, see 2–11 September during Leslie and 17–19 October during Gonzalo) and azimuthally progressive (i.e., signals continuously changing in direction of arrival, see 11–13 September during Leslie and 19–20 October during Gonzalo); (b) Both signals can be associated with sections of the hurricane tracks remarkably well, the former appearing as the hurricane intercepts the 160–165° backazimuth range for both hurricanes and remaining active for a couple of days after the true hurricane backazimuth significantly changes, while the azimuthally progressive signals have a noticeable spatial shift directed toward the rear rim of the hurricane as it moves northwards. This is particularly clear for both Rayleigh and Love waves during Gonzalo (Figures 3d and 3f). (c) While the BP maxima are aligned with the hurricanes considered, no clear correlation exists for the simultaneously active cyclones (light blue-colored dots in Figures 3c and 3e) occurring farther away but within the zone of influence of the main hurricane (at $\lesssim$4,000 km), so that their contribution to the total BP is negligible; and (d) Rayleigh and Love waves are both generated by the hurricane at about the same time arriving from about the same direction, while having different coherency levels (absolute BP values are generally higher for Rayleigh waves and have thus a higher contrast with respect to the background levels) and different statistical distributions in time and space (Rayleigh maxima tend to be less scattered than Love wave maxima).

Consistently with the first observation, it can be hypothesized that the azimuthally constant signals (from now on termed "steady") are related to fixed regions in the ocean that are "activated" as the hurricane passes nearby, remaining active for some days after it moves away. On the other hand, the source of the azimuthally progressive microseismic signals (from now on termed "progressive") would trail behind the hurricane and is detected as the later approaches the coast located closest to the array. As a way of comparison, the mean and maximum significant waveheights over 4 × 4 degs-regions centered at Bermuda island in the Sargasso sea and the Gulf of Maine near the US-Canada border are shown in Figures 3g and 3h. Both regions lie along the observed azimuthally stable direction of 160–165° from the QC array and contain shallow water depths as well as a variable topography at depths of 2–4 km presumably needed to generate strong PM and SM signals, respectively (see e.g., Tanimoto (2013) for optimal SM generation depths). The remaining seafloor along this azimuthal direction is mostly deeper and less topographically diverse. The waveheights at the Gulf of Maine remain relatively low and stable during the passage of both hurricanes, while those at Bermuda increase by several meters correlating with the onset of the steady PM signal. However, it is also observed that the microseismic signals continue to be generated from the same direction even after the waveheights decay, such that another source location centered elsewhere along the steady backazimuth line could exist. Based on the assumption that PM is generated by the largest wave heights (at shallow water depths), an expected azimuthal distribution of sources can be obtained from the waveheight hindcasts (Figures 3i and 3j) which shows a partial agreement between the seismic and the hindcast data, as high waveheights occur beneath the hurricane track, as expected. However, according to the hindcast model the maximum waveheights occur approximately under the eye of the cyclone and not in the rear quadrants as the seismic data suggest, while at the same time not all the BP features are clearly represented in the hindcast data and vice-versa.

5.2. Leslie and Gonzalo—Secondary Microseisms

Apart from small backazimuth fluctuations, the general distribution of SM (in the band 0.10–0.16 Hz) Rayleigh and Love wave BP values are comparable (Figures 4a–4d), although a few arrivals of one wave type are occasionally not evidenced in the other. The steady and progressive BP signatures are still evident for both hurricanes and are similar to those of PM, yet there appears to exist a noticeable variability in direction of arrival of the main

Figure 3. Summary of results for Leslie (left column) and Gonzalo (right column) in the PM band (0.05–0.09 Hz). (a and b) Spectrograms with 256 s-PSD time window and 60% overlap. BP as a function of time and backazimuth at QC array for (c and d) Rayleigh and (e and f) Love waves with white dashed lines indicating the closest approach to QC. True bearings at regular time steps toward the eyes of Leslie (Gonzalo) are shown as red (orange) dots (their saturation is proportional to maximum sustained windspeeds), while the backazimuth toward the cyclone rims (ROCI) are marked by the dashed red lines. Simultaneous hurricanes located farther away are shown as pale blue dots. The mean and maximum significant waveheights over a 4 × 4 earth degs-square centered at Bermuda and the Gulf of Maine (g and h) were estimated to retrieve their average wave activity, as these regions are potential sources of the observed microseisms. Maximum waveheights observed along 4,000 km-radius lines away from the QC array (approx. max. distance to the hurricanes from QC) (i and j) are shown for comparison overlaid by the same Rayleigh BP maxima of (b and c) (respectively) as white dots. Notice the different time scales shown for each hurricane.

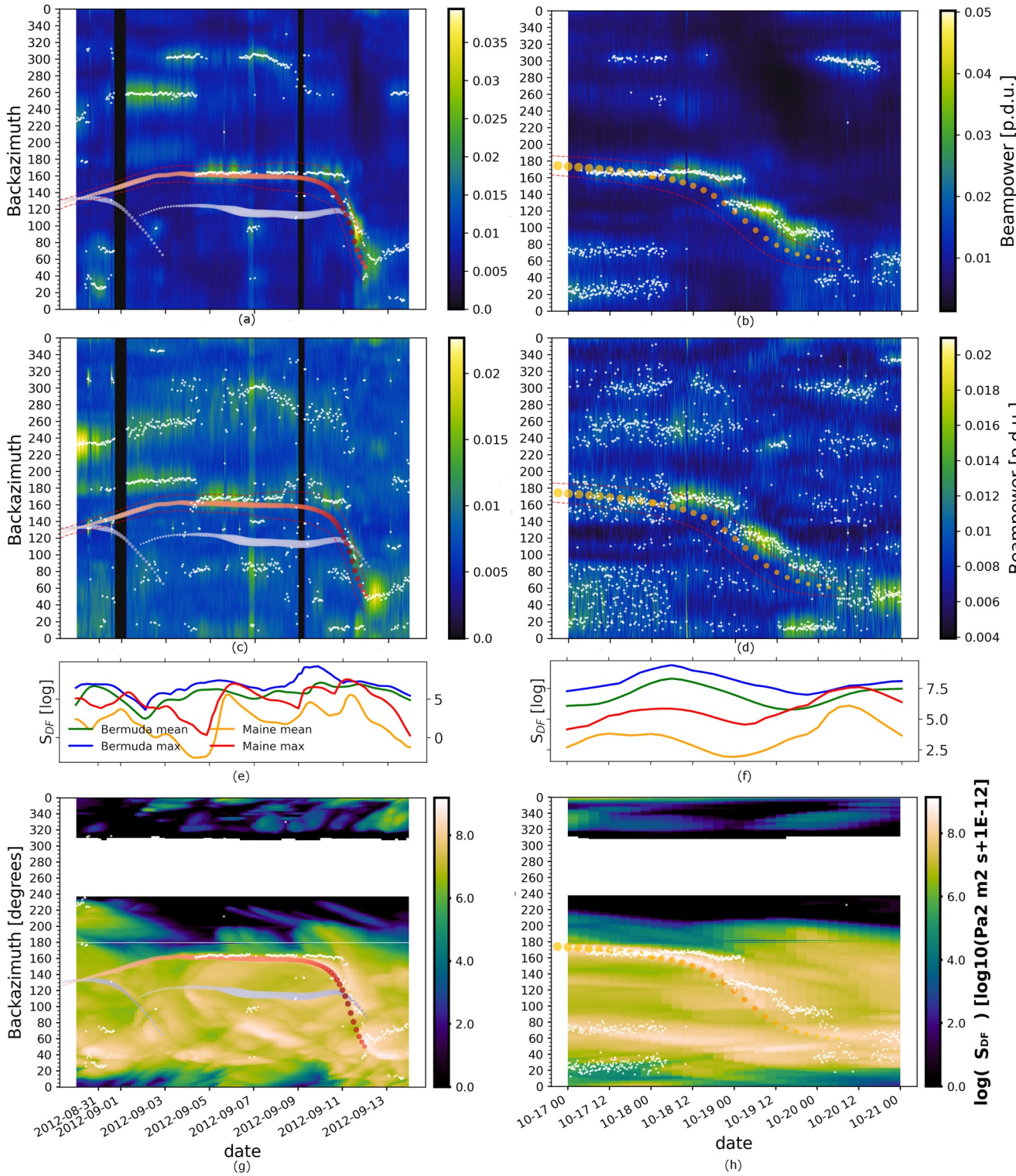

Figure 4. Summary of results for Leslie (left column) and Gonzalo (right column) in the secondary microseisms band (0.10–0.16 Hz) following the scheme of Figure 3. BP as a function of time at QC array for (a and b) Rayleigh and (c and d) Love waves. The (logarithmic) mean and maximum S_{DF} values in 4 × 4 degs-square surfaces at Bermuda and the Gulf of Maine are shown for comparison (e and f). The maximum S_{DF} values observed within a distance of 4,000 km in the respective azimuthal direction from QC array (g and h) are shown for comparison, overlaid by the same Rayleigh BP maxima of (a and b) (respectively) as white dots.

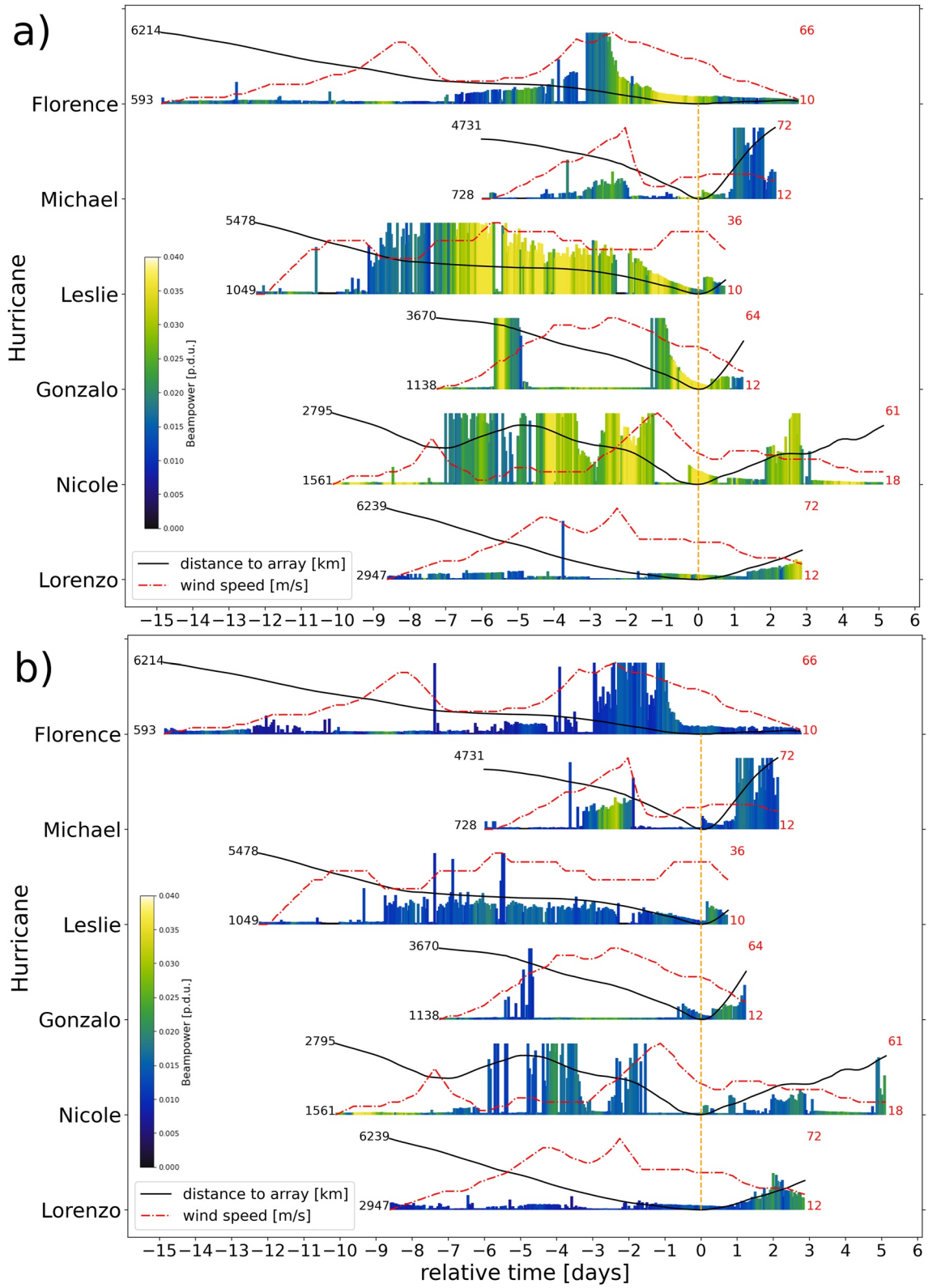

Figure 5. Agreement between expected/observed backazimuths of the BP maxima relative to the bearing toward the eye of each hurricane (as the height of each bar—see Section 5.3 for detailed description) for (a) Rayleigh and (b) Love waves in the PM band. Data is aligned relative to the closest approach of each hurricane to the QC array (vertical orange lines). Distances between the array and hurricane center as continuous (black) lines and maximum sustained wind speeds in (red) dotted-dashed line. The values of largest and smallest distances (maximum windspeeds) during the study interval are given to the left (right).

hurricane microseisms, being slightly higher for SM in comparison to PM. The S_{DF} variable is shown here for comparison instead of waveheights, as SM are expected to result from non-linear SGW interactions. Similarly to the waveheights and the corresponding PM results, higher S_{DF} values are observed at Bermuda as the steady signals occur relative to the Gulf of Maine (Figures 4e and 4f), while the S_{DF} values in the latter increase during the very last days as the hurricanes approach the Grand Banks off Newfoundland. However, the correlation for SM is not as striking as for the PM results in Figures 3g and 3h. The azimuthal distribution of S_{DF} (Figures 4g and 4h) shows a more scattered distribution of sources which is consistent with the higher variability of maxima in Figures 4a–4d. A good consistency between the hurricane tracks and the maximum S_{DF} values exists, while these overlap in time with the steady microseismic signal (4–11 September for Leslie and 17–18 October for Gonzalo in Figures 4g and 4h). Here however, a noticeable backazimuth lag between the eye of the hurricane and the maximum S_{DF} values exists during the last days of both hurricanes, as can be seen in the progressive BP signature as well (white dots in same Figures).

5.3. Temporal and Azimuthal Distribution of Hurricane Microseisms

In order to visualize the temporal distribution of BP signatures for all the hurricanes considered, Figure 5 summarizes the BP values (color-coded) and the degree of agreement between observed and expected backazimuths, calculated as $\beta_0/(\Delta\beta + 1)$, that is, the inverse of the deviation between the (true) backazimuth toward the eye of each hurricane and that of the global BP maximum for PM at each time step ($\Delta\beta$) using $\beta_0 = 4°$ as a reference normalization value for all hurricanes, so that backazimuth errors of this order or less are exaggerated. Rayleigh waves (Figure 5a) show higher BP values than Love waves (Figure 5b), which could be explained as a higher coherency of the wavefield of the former (or lower S/N ratio of the two-component transversal polarizations). The results for SM are similar in distribution but on average much lower in absolute BP values. The latter are included in Figure S2 of Supporting Information S1.

From Figure 5 it can be observed that in overall no clear correlation exists between the hurricane category and the degree of observed/true track agreement. Particularly, hurricanes Gonzalo, Nicole, and Lorenzo do not show a good correlation, while Florence and Michael only show partial correlation for a few days. Hurricane Leslie has high levels of backazimuth agreement along its lifetime, but its intensity (category) variations are not clearly reflected in its seismic response. However, this agreement is only apparent from the perspective of a single array. The highest BP values do not necessarily match timespans with the highest observed/expected backazimuth agreement nor with those having the highest hurricane category. Figures 5a and 5b indicate a low agreement in azimuthal directions as obtained from BP maxima and the meteorological center of the hurricane during closest approach to the array, which is explained by the fact that the detected signals often point toward the trail of the hurricane, as discussed in Sections 5.1 and 5.2. However, high Rayleigh wave BP values tend to occur shortly before and during the closest hurricane approach (Figure 5a), indicating reliable signals. This is not as obvious for Love waves (Figure 5b). The higher coherency of PM Rayleigh relative to Love waves might be due to the fact that there is generally more coherent Rayleigh wave energy in this frequency band and the large deviation at the closest hurricane approach to the array could correspond to the fact that the signals are not generated at the center of the hurricane but at some other region away from it. It is also worth noting that low track agreements where the smallest inter-distances exist do not necessarily indicate bad correlations, having in mind that large objects cover a wider range of backazimuths the closer they are to the observation point. In general, it is confirmed from Figure 5 that coherent microseismic signals likely related to hurricanes only occur intermittently and not along their whole trajectories.

The maximum BP value in each azimuthal direction during the entire lifetime of each hurricane (global BP maxima of beamforming plots as those of Figures 3c–3f and 3a–3d) are depicted in Figure 6. This figure summarizes the azimuthal distribution of the most coherent microseismic signals observed during all hurricanes considered. For PM Rayleigh and Love waves (Figures 6a and 6c), well-defined BP maxima with back-azimuths toward the Atlantic ocean (marked by dashed black lines) stand out for hurricanes Leslie and Gonzalo as well as for most of the other hurricanes. In particular, the ∼165° direction belonging to the steady signal tentatively linked to Bermuda island described for Gonzalo and Leslie in Sections 5.1 and 5.2 is also present for the remaining hurricanes and for both, Rayleigh and Love waves. Recurrent signals at 30–60° occur likewise during each hurricane. Other representative backazimuths only exist for some of the hurricanes, but some prominent directions are clearly discernible.

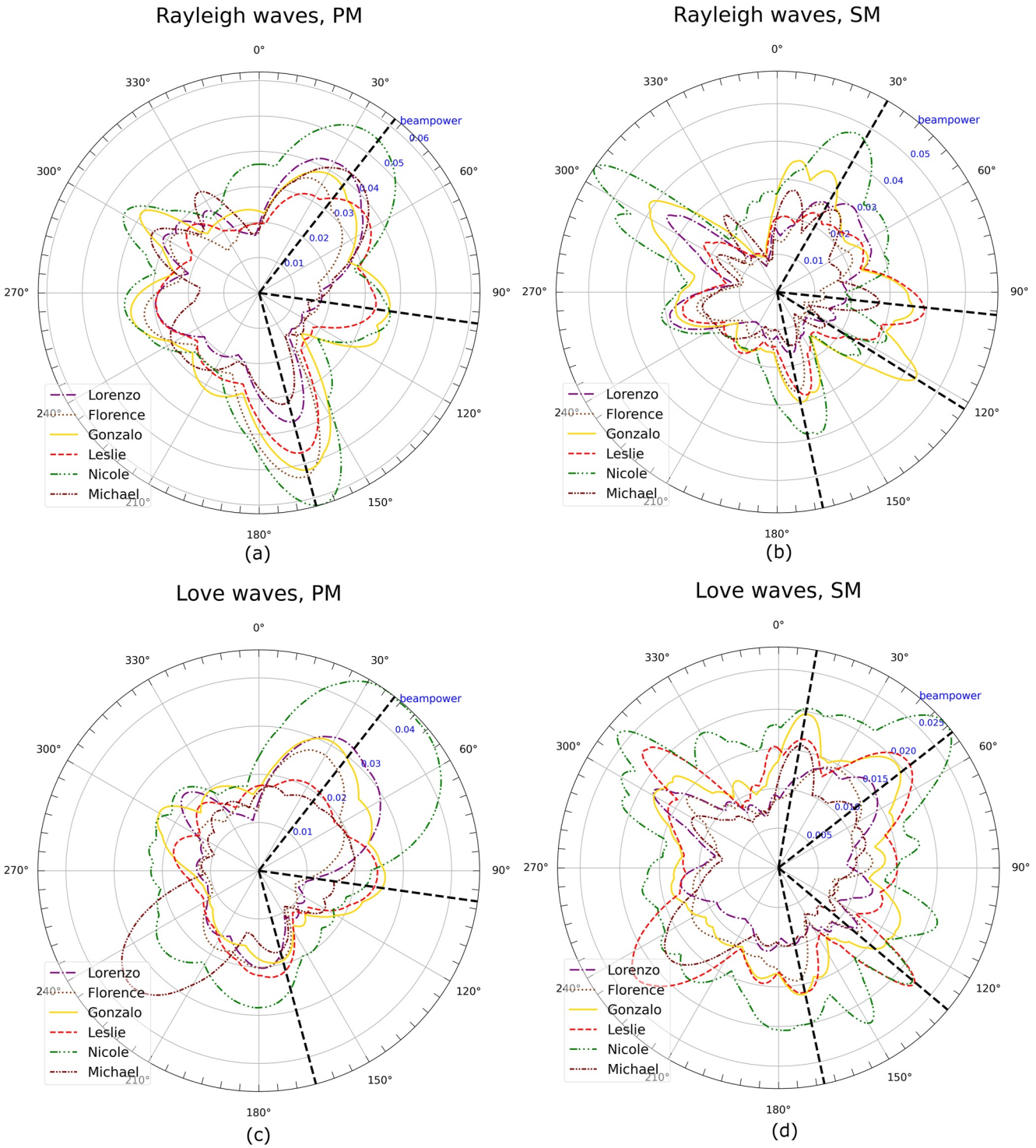

Figure 6. Azimuthal distribution of maximum BP values observed at QC array during the lifetime of each hurricane, after averaging over the corresponding frequency range in the (a and c) PM and (b and d) secondary microseisms bands. Results are given for Rayleigh and Love waves (upper and lower row, respectively). Some of the most coherent arrivals for Leslie and Gonzalo (and also for the remaining hurricanes) looking toward the Atlantic ocean are marked with black dashed lines. Note that the radial BP scales (in blue) were adjusted for each plot.

SM maxima (Figures 6b and 6d) exhibit a higher spatial variability, but prominent backazimuths also occur that barely match between Rayleigh and Love waves. Notice that the BP value range (in blue) is considerably smaller for the latter in comparison to the former, implying that Love waves have BP values that are closer to the noise floor and are thus more likely to be affected by random fluctuations. This observation applies as

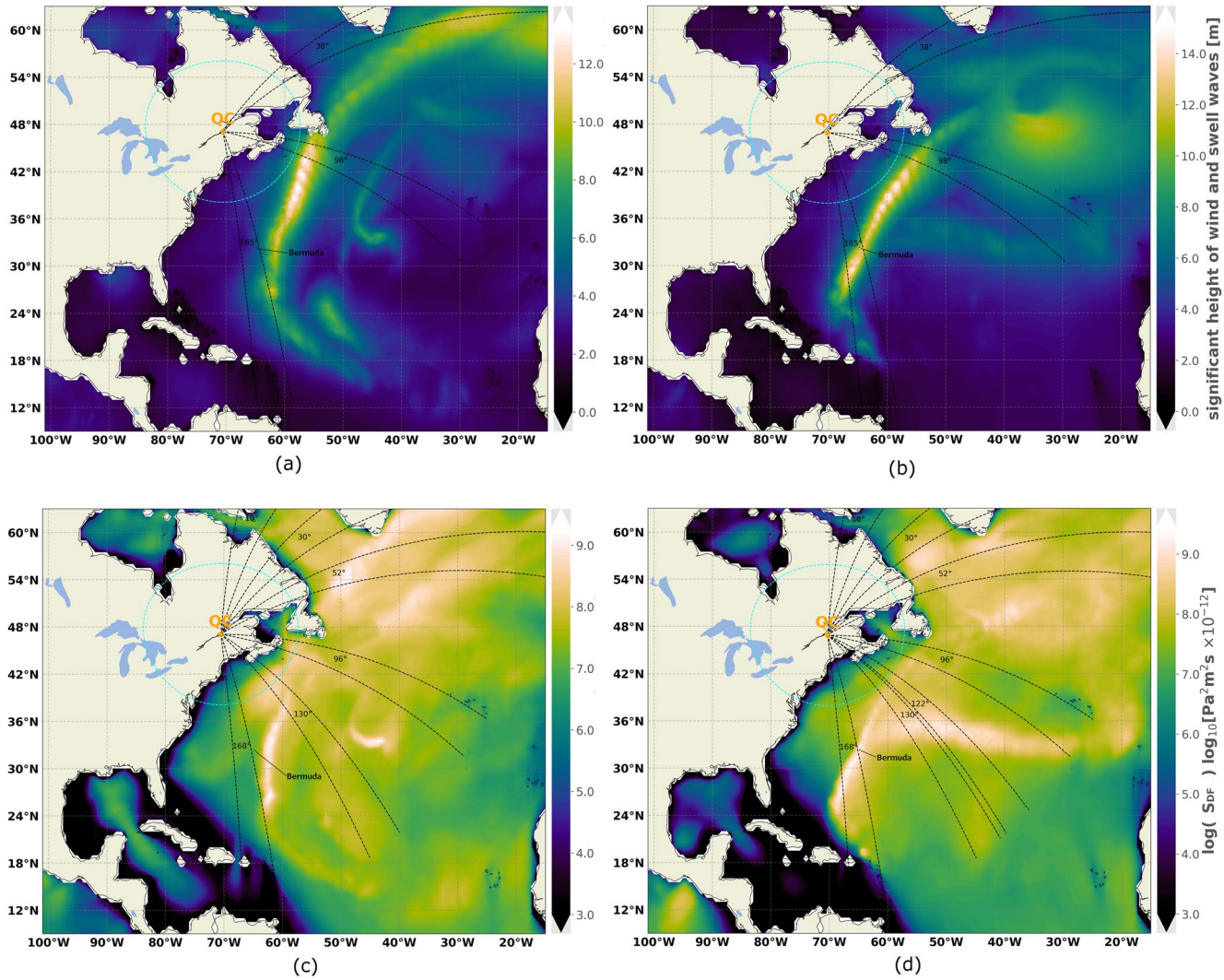

Figure 7. (a and b) Significant waveheights and (c and d) S_{DF} maps for (a and c) Leslie and (b and d) Gonzalo with the prominent directions of arrival of Figure 6 represented in ±5°-sectors and 4,000 km-long lines (black dashed). For scale reference, a 1,000 km-radius around the QC array is shown in cyan (comparable to the maximum distance found in Section 5.1).

well to the (low) BP values of some hurricanes relative to others (e.g., Florence and Michael relative to the others).

It follows from Figure 6 that the surface wave microseisms that occur during major hurricanes are bounded to some fixed directions. This is particularly clear for PM, while at the same time a higher azimuthal variability exists for SM, in accordance with the fact that the latter could theoretically be generated over a larger set of oceanic regions, and not only near the coast, as expected for PM. Rayleigh wave signals are more stable and consistent with specific directions of arrival in comparison to Love waves for both the PM and SM bands.

The maps in Figure 7 synthesize the observations in Figures 5 and 6 for hurricanes Leslie (Figures 7a and 7c) and Gonzalo (Figures 7b and 7d) and additionally depict hindcast data averaged over the timespan of the hurricanes. Large significant waveheights (Figures 7a and 7b) at or near coastal/shallow waters indicate regions where efficient PM generation is expected, while large S_{DF} values (Figures 7c and 7d) are in principle expected where the strongest SM are excited. The tracks of the hurricanes are partially observed as aligned maxima in the hindcast data and the higher variability of SM sources in comparison to PM observed in Figures 6b and 6d is also apparent in the S_{DF} maps in comparison to the waveheights.

The backazimuths corresponding to the BP maxima in Figure 6 are shown in Figure 7 with a 5° uncertainty range. These backazimuths show a rather low correspondence with regions where the maximum waveheights

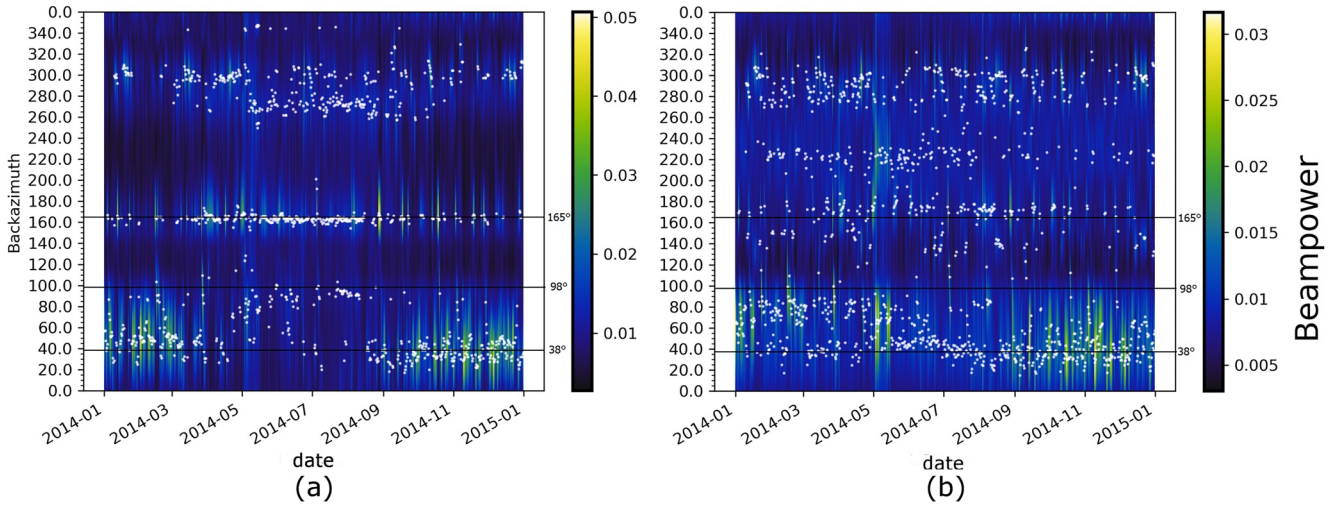

Figure 8. Beampower plot in backazimuth-time space for primary microseisms (PM) in 2014 averaged at 1-day timesteps for (a) Rayleigh and (b) Love waves. The prominent PM backazimuths of Figures 6a and 6c are marked for comparison. White dots represent BP maxima.

(or S_{DF}) occur. In fact, some of the beamforming maxima point toward regions with low mean oceanic anomaly along distances of more than 4,000 km. Apart from the continental platform of North America, islands and seamounts in the Sargasso sea and the Caribbean, most ocean depths in the western North Atlantic exceed 4 km (Figure 1), which can be a factor for preventing the excitation of sufficiently strong microseisms. Conversely, some of the regions with high SGW anomaly are not represented in the beamforming analyses, which would only be consistent for weak teleseismic sources or exceedingly deep waters in the case of PM but not otherwise. On the other hand, some of the observed seismic sources do match locations where high wave heights and S_{DF} values occur, for example, the ∼52° and ∼98° backazimuths crossing the Labrador sea and the Grand Banks of Newfoundland, respectively, during Leslie, or the steady signal at ∼168° near the Sargasso sea. As discussed in Sections 5.1 and 5.2, it is confirmed that the most likely location of the steady source along the ∼165° backazimuth line is somewhere near Bermuda island, where high waveheights as well as S_{DF} anomalies occur as opposed to the Gulf of Maine, which is the closest shoreline along that line but has very low mean SGW amplitudes.

In summary, our beamforming results indicate that cyclone-related microseismic signals are only excited at particular locations roughly sourced toward the apparent location of the corresponding cyclone, as if microseism generation regions were "activated" by the latter. Figure 8 depicts a full-year beamforming analysis at QC array. It can be seen that particularly for Rayleigh waves (Figure 8a) consistent directions of arrival occur throughout the whole year and not only between June and October, which corresponds to the North Atlantic hurricane season. For instance, the ∼165° steady microseismic source observed for several hurricanes and outlined in Figures 6a and 6c is most active during the Northern hemispheric summer, but also remains active and stable at other times of the year. The same applies for other backazimuth ranges where beampower (BP) maxima tend to cluster. Similarly, the ∼38° source is most active during the northern hemispheric winter season, while the ∼98° source pointing toward Newfoundland is only sporadically active throughout the year for no more than a couple of days in a row. The Love wave BP maxima (Figure 8b) are more scattered, variable and often do not match the direction of arrival of those for Rayleigh waves, but the general picture and the seasonal variations remain the same. The ∼38° and ∼165° steady sources can also be traced for Love waves albeit with less continuity than for Rayleigh waves.

6. Discussion

We observe hurricane-generated microseismic Rayleigh and Love waves originating from the North Atlantic at a virtual seismometer array in Canada in both the PM and SM bands. These microseisms manifest as intermittent signals that are not continuously generated at the center of the active cyclone and are potentially radiated non-uniformly and/or significantly attenuated depending on the point of observation.

6.1. Love and Rayleigh Cyclone Microseisms

Our results argue in favor of nearly colocated sources of cyclone-related microseisms for Love and Rayleigh in both PM and SM bands, suggesting common forcing mechanisms and/or a strong site control. This observation is supported by Nishida et al. (2008), Juretzek and Hadziioannou (2016), and Juretzek and Hadziioannou (2017), who made similar observations with respect to the main microseismic Love and Rayleigh wave sources. Matsuzawa et al. (2012) conclude that moderate deviations exist between the Rayleigh and Love wavefield source areas, while acknowledging that the arrival directions of both are similar. Gal et al. (2017) investigated the background microseismic Rayleigh and Love wavefield in the upper limit of the SM band (0.35–1 Hz) and observed a markedly distinct spectral and azimuthal distribution of each, Love waves correlating with near-continent sedimentary basins while Rayleigh waves correlating with convex coastlines.

The observed backazimuths of Love wave BP maxima tend to have a higher variance and less continuity than those of Rayleigh waves, while the latter have smoother, less scattered and in general less diffuse signatures. This is in agreement with a Love wavefield generated over a comparatively broader generation area or resulting from complex radiation patterns due to a strong influence of heterogeneities and/or propagation effects. Previous works have explained this observation in terms of scattering, wave conversions and diffractions (Juretzek & Hadziioannou, 2017; Ziane & Hadziioannou, 2019), or interactions with heterogeneous 3-D subsurface structure (Gualtieri et al., 2021).

Love waves in the SM band generally show the lowest absolute beampower values, indicating a lower coherency of the wavefield or a relative abundance of uncorrelated Love wave noise in this frequency band. A generally higher coherency of Rayleigh over Love waves was also observed in the PM band, in contrast to previous studies that have presented evidence of dominant Love waves as well as high H/V ratios of PM (Becker et al., 2020; Friedrich et al., 1998). This could be explained by the fact that seismic energy from SM sources with low frequencies (of about 0.08 ∼0.09 Hz) due to the high winds and the resulting long period SGWs might "leak" into the PM band defined here (0.05–0.09 Hz), contributing to increase the BP of PM Rayleigh waves. This energy leakage however seems to be more likely to occur the other way round, considering that highly coherent SGW with frequencies as low as ∼0.04 Hz (half of 0.08 Hz) are relatively uncommon even for hurricanes (and thus unlikely to generate strong SM signals), whereas coherent SGW at higher frequencies ($f \gtrsim 0.1$ Hz) may leak PM energy into the SM band considered here (0.10–0.16 Hz). An alternative interpretation is that cyclones could efficiently excite Rayleigh waves in the PM band. Such efficient Rayleigh wave excitation could be site-dependent, as the maximum values occur only at well-defined backazimuths, even in the longer term, as depicted in Figure 8. The higher energy of microseismic Rayleigh over Love waves in the SM band has been reported by Nishida et al. (2008) and Tanimoto et al. (2016). We are unaware of other observations of dominant Rayleigh over Love microseismic waves in the PM range.

6.2. Primary and Secondary Cyclone Microseisms

The source area colocation of PM and SM suggested by our results is also pointed out by Cessaro (1994) and Nishida et al. (2008), while several studies argue that PM are only linked to shallow areas, while SM can be generated in the deep ocean as well. We note however, that the background microseismic wavefield resulting from swells and wind regimes acting over broader oceanic regions and longer time scales could differ from the microseismic wavefield linked to the more spatially localized and short-lived cyclone winds and their corresponding highly directional swells.

An additional observation is that the agreement of beamforming results between Rayleigh and Love waves in the same frequency band is often better relative to the agreement that there is for the same wave type between different frequency bands. The similarity is particularly obvious for Love and Rayleigh waves in the PM band, which suggests a coupled generation mechanism for both wave types in this frequency band. On the other hand, SM features tend to show stronger backazimuth variability of Love relative to Rayleigh waves, suggesting marked differences in the generation of each wave type in the SM band. A similar observation is outlined in Juretzek and Hadziioannou (2017). Alternatively, the higher variation in the SM frequency band may relate with high frequency PM leaking into the SM band, as explained above.

6.3. Directional Distribution of Cyclone Microseisms

Cyclone-related signals with steady (fixed backazimuth) as well as progressive (shifting backazimuth) signatures were identified. While the steady signal might only be apparent (as we only evaluate a single array), its recurrent backazimuth-invariability over long timespans is remarkable and contrasts with the changing bearing toward the hurricane tracks that triggered them. The azimuthally progressive signals are recognized during timespans with high surface wave wavefield coherency, having bearings that coincide with or consistently lag behind the true backazimuths toward hurricanes Gonzalo and Leslie, suggesting a potential source lying in the rear quadrants or along the wake of the hurricanes. The latter observation has been pointed out in several studies (Chevrot et al., 2007; Chi et al., 2010; Davy et al., 2014; Farra et al., 2016; Lin et al., 2017; Park & Hong, 2020). Altogether, the idea of a forcing region of microseisms "behind" storms was suggested by Tabulevich (1971) and is implicit as well in the class IIIa source mechanism of SM (see Ardhuin et al., 2011), suggested originally by Longuet-Higgins (1950), in which the backwards propagating wind waves at the wake of a storm interact with the forward swells generated in previous times if the system moves fast enough. Interestingly, the observed PM signals for the hurricanes show the same spatial delay as the SM signals. For PM frequency band Rayleigh waves this might be explained by leaking of SM energy with low frequencies into the PM frequency band or would alternatively suggest that the non-linear SGW self-interaction mechanism (or the interaction with reflected SGW or distant swells) might not be necessary to explain the trailing SM signals. In any case, a strong site control agrees with the uniformity of the beamforming results for all wave types in the microseismic band.

6.4. Microseisms During Cyclone's Advance Into Shallow Waters

Strong sources are observed as the hurricanes approach the shallow-water regions over the continental platform. This was observed during the landfall of Florence; the re-entry of Michael into the Atlantic; or on 16 October during Nicole, in which a prominent signal was seen as its track approached the protruding edge of the continental slope (Figure S3 in Supporting Information S1, Supporting Information). The progressive microseisms observed during the approach of hurricanes Gonzalo and Leslie to the Great Banks of Newfoundland and its continental slope also support this observation and were confirmed via independent P-wave ray tracing (not shown). Microseisms generation in shallow bathymetry was also observed by Essen et al. (2003), Bromirski et al. (2013), and Ying et al. (2014). Guo et al. (2020) studied Rayleigh waves in the eastern North American margin and found that PM (0.050–0.085 Hz) are likely distributed along the continental shelf and adjacent deep ocean areas (in our study these seem strongly related to shallow waters too), while the long-period SM (0.1–0.2 Hz—attributed to distant swells) occurred in deep ocean regions near the continental slope. Other authors also report on the deep ocean origin of SM (e.g., Beucler et al., 2015; Gualtieri et al., 2015; Zhang et al., 2010). Based on our results, the existence of deep-ocean-generated microseismic signals strong enough to be detected inland cannot be ruled out neither be supported.

Previous microseismic studies in the Atlantic ocean had shown prominent seasonal PM and SM body wave sources South of Greenland and Iceland around winter as well as SM along the North American Atlantic coast with lesser activity during summer (Euler et al., 2014; Gerstoft et al., 2008; Kedar et al., 2008; Landès et al., 2010). Traer et al. (2012) also observed PM and SM sources during summer and winter along the western Atlantic margin, as well as off Newfoundland and South of Greenland and the Labrador sea. Fan et al. (2019) studied Z-component records in the band 0.02–0.05 Hz (below the here defined PM range) and reported microseismic source areas compatible with those found by us at the Great Banks of Newfoundland parallel to the shelf break offshore Nova Scotia in front of the Saint-Lawrence river bay during hurricane Gonzalo in both its rear quadrants on 19 October 2014 (a C1 hurricane at the time), between 6:00 and 9:00a.m. (compare Figures 7b and 7d with Figure S4 in Supporting Information S1, which includes a modified version of the original Figure 3e in Fan et al. (2019)). These microseisms roughly match the Rayleigh and Love wave BP peaks observed here in both the PM and SM bands and occurring in the same region at the same times (Figures 3d, 3f, 4b, and 4d). It is worth noting that these types of signal were not detected as Gonzalo was farther away from the QC array and having an even higher category (>2). In Fan et al. (2019), the traced sources also do not occur where the maximum waveheights are, but rather in the rear quadrants of Gonzalo as well as outside of the main wind influence area, slightly more numerous to the left of the path (in the movement direction), around an area in which a gradient of wave heights exists and where the main wave direction was perpendicular to the shelf line (Figure S4a in Supporting Information S1). The sources found in that study seem to be primarily controlled by the shape of the shelf break instead of the shape of the waveheight anomaly.

Our results show signals related to Gonzalo that continue to exist further north up to the coast off Newfoundland, entering Labrador Sea, all along the continental platform (Figures 3d, 3f, 4b, and 4d). It is unclear if these are generated along the continental slope break or over the flat continental shelf. The discontinuity and slight decrease in BP values observed for SM Rayleigh and Love waves during Gonzalo on 19 October at 12:00 (Figures 4b and 4d) coincides with the translation of the microseismic source area from the shelf break onto the continental platform. Rayleigh waves continue to be clearly detected afterward, while Love waves become somewhat scattered and weak. This suggests that SM Love waves are amplified mostly along the inclined shelf slope, probably due to the rugged relief and/or complex layering structures, which are thought to be efficient generators of Love and converted waves (e.g., Le Pape et al., 2021; Nishida, 2017; Tanimoto et al., 2016; Ziane & Hadziioannou, 2019). At the same time, prominent PM signals for both Rayleigh and Love waves appear as the source area moves onto the continental slope (Figures 3d and 3f), as expected from the shallow generation of PM. The potential use of microseisms for imaging of shallow sedimentary layers is thus evoked.

6.5. Observational Limitations and Inconsistency With Hindcast Data

In this study, a single array with optimal aperture and geometry was implemented. Multiple combined (optimal) arrays are generally expected to provide additional spatial constraints and potentially an increased accuracy for microseismic source tracking. However, our beamforming tests on other virtual arrays adjacent to the hurricane tracks in the North Atlantic did not lead to comparable results as for the QC array and thus prevented the localization of microseismic source regions by triangulation (see Text S1 and Figure S1 in Supporting Information S1 for details and beamforming results of some of the discarded virtual arrays). The cause of the latter result is not yet fully clear. Non-uniform radiation patterns, strong attenuation at large distances and/or local noise contamination are potential factors limiting an spatially distributed approach. In a similar way, the results of Ward Neale et al. (2018) and Wang et al. (2021) also yielded unsatisfactory combined-image beamforming triangulation of microseismic sources using multiple distributed arrays, as the authors acknowledge that some microseismic signals that were detected at some arrays were not properly detected at others. The aforementioned studies as well as ours, call for further research to clarify and characterize in detail the microseismic wavefield radiation and the propagation effects of ocean microseisms.

The oceanic regions with largest mean waveheights or S_{DF} values during each hurricane were not always highlighted by prominent BP maxima, which in turn often pointed toward regions with low oceanic anomalies, if present at all (see Figure 7). Added to water depth, further physical parameters that combine with the SGW forcing might play a relevant role in the observed microseismic signals. Candidates include: seabed morphology at wavelength scale; subsurface lithology and structure; oceanic mesoscale phenomena and structure, or other factors not yet considered. As a way of example, Sepúlveda et al. (2005), Rodgers et al. (2010), Khan et al. (2020), amongst others, outline how surface wave (de-)focusing can occur due to reflections in topography such as ridges and mountain tops, being a possible contributing factor for microseisms amplification at the continental slope. The role of sediment material, layering and/or thickness in microseismic phenomena has been addressed in the works of Tanimoto and Rivera (2005), Tanimoto et al. (2016), Fan et al. (2019), and Gualtieri et al. (2021).

7. Conclusions

Cyclones wandering over the ocean generate distinct microseismic waves that can be detected at land stations. These microseisms occur for both retrograde Rayleigh and Love waves in the microseismic frequency band, from about 0.05 to 0.2 Hz. A significant observation is that these signals are not excited equally during the entire lifetime of the cyclone but instead as semi-continuous signals at specific oceanic locations as the cyclones are passing by, hampering a continuous cyclone-tracking via far-field arrays. Similar observations have arisen from previous studies (e.g., Park & Hong, 2020).

Apart from differences in BP levels and distribution of maxima, cyclone-related Love and Rayleigh wave sequences tend to occur simultaneously and roughly match each other in direction of arrival quite well in most scenarios, particularly in the same frequency band, suggesting a colocation of the generation area and a strong local (site) control. However, the recorded Love wavefield is more diffuse and less coherent or weaker, while the recorded Rayleigh waves are more coherent and focused. The sharpest and most accurate cyclone trackings were obtained for Rayleigh waves in both the primary (PM) and secondary (SM) frequency band. Both wave

types were most efficiently excited at fixed shallow regions including the continental slope and shallow shelf off Newfoundland, virtually independently of storm category. No cyclone microseisms were safely linked to deep open ocean regions. However, the restriction to one single onshore array potentially hampers the detection capability for deep, distant microseismic sources.

Two types of cyclone-related signals were identified: azimuthally steady (constant) and azimuthally progressive. The latter appear to occur at the trail of cyclones, suggesting that wind waves in the rear quadrants and cyclone-originated swells play a significant role in the microseismic generation, likely providing an optimum surface gravity wave (SGW) directional spectrum. Occasionally, the passage of cyclones over or nearby oceanic regions where microseismic generation appears to be highly efficient triggers strong steady signals that can last several days.

The existence of prominent microseisms related to cyclones such as those observed in our study at specific oceanic regions is inviting for passive imaging and monitoring, in particular considering that forecasts of the tracks of cyclones are pre-available via accurate meteorological models. Our results further indicate the need to study in more detail the radiation patterns, attenuation and the complexity of the cyclone microseismic wavefield propagation. Near-field (on- and off-shore) observations using widespread and dense sensor layouts, such as large-N-arrays, OBS, floating seismographs (e.g., MERMAIDS—see Hello and Nolet (2020)), or Distributed Fiber Optic Sensing, might be particularly adequate to cover some of these aspects. Generally speaking, an improved detection and understanding of ocean microseisms has the potential to refine existing atmosphere-ocean-solid earth coupled models, and eventually to bring complementary information to traditional methods for cyclone monitoring and tracking in the ocean.

Acronyms

ARF	Array response (transfer) function
BP	Beampower
DF	Double frequency (related to non-linear interactions of surface gravity waves traveling in opposite directions)
OBS	Ocean-bottom seismometer(s)
PM	Primary Microseism(ic)
PSD	Power spectral density
QC	Reference to the virtual array in Québec, Canada implemented in this study
SGW	Surface gravity wave(s)
SM	Secondary Microseism(ic)
SNR	Signal-to-noise ratio
ROCI	Radius of outermost closed isobar of a cyclone
WWSSN	World-Wide Standardized Seismograph Network

Data Availability Statement

The Atlantic cyclone data was obtained from http://ibtracs.unca.edu/ (Knapp, Applequist, et al., 2010). The seismic data was recorded by seismometers of the Canadian National Seismic Network (Natural Resources Canada (NRCAN Canada), 1975) which is found at https://www.fdsn.org/networks/detail/CN/ and was freely accessed through the IRIS client (http://ds.iris.edu/ds/) of the International Federation of Digital Seismograph Networks server (https://www.fdsn.org/). Stations for the virtual array were selected using the Wilber 3 system of the IRIS consortium (http://ds.iris.edu/wilber3/). Wavewatch III (Tolman et al., 2014) hindcast data was downloaded from the French Research Institute for Exploitation of the Sea (IFREMER, https://wwz.ifremer.fr/) at ftp://ftp.ifremer.fr/ifremer/ww3/HINDCAST, and bathymetry from GEBCO (GEBCO, 2003). The 3C-Beamforming script was developed by Carina Juretzek (Juretzek & Hadziioannou, 2016). Seismic data downloading, processing and plotting of results relied mainly on Obspy (Beyreuther et al., 2010) (https://docs.obspy.org/). Several other Python standard libraries and modules for scientific computing were implemented (e.g., Numpy, Scipy, Matplotlib, Cartopy, Colorcet, and Cmocean).

Acknowledgments
This work was partially funded by the Emmy Noether program (HA7019/1-1) of the German Research Foundation (DFG). We would like to thank N. Nakata, S. Kedar, and one anonymous reviewer for their useful suggestions to improve our manuscript. J.P.Q would like to thank the authors of all the previous works upon which ours was based and the corresponding sources that made them available. Open Access funding enabled and organized by Projekt DEAL.

References

Ardhuin, F., Gualtieri, L., & Stutzmann, E. (2015). How ocean waves rock the Earth: Two mechanisms explain microseisms with periods 3 to 300 s. *Geophysical Research Letters*, *42*(3), 765–772. https://doi.org/10.1002/2014gl062782

Ardhuin, F., Stutzmann, E., Schimmel, M., & Mangeney, A. (2011). Ocean wave sources of seismic noise. *Journal of Geophysical Research*, *116*(C9), C09004. https://doi.org/10.1029/2011JC006952

Barruol, G., Davy, C., Fontaine, F. R., Schlindwein, V., & Sigloch, K. (2016). Monitoring austral and cyclonic swells in the "Iles Eparses" (Mozambique channel) from microseismic noise. *Acta Oecologica*, *72*, 120–128. https://doi.org/10.1016/j.actao.2015.10.015

Becker, D., Cristiano, L., Peikert, J., Kruse, T., Dethof, F., Hadziioannou, C., & Meier, T. (2020). Temporal modulation of the local microseism in the North Sea. *Journal of Geophysical Research: Solid Earth*, *125*(10), e2020JB019770. https://doi.org/10.1029/2020JB019770

Beucler, E., Mocquet, A., Schimmel, M., Chevrot, S., Quillard, O., Vergne, J., & Sylvander, M. (2015). Observation of deep water microseisms in the North Atlantic Ocean using tide modulations. *Geophysical Research Letters*, *42*(2), 316–322. https://doi.org/10.1002/2014GL062347

Beyreuther, M., Barsch, R., Krischer, L., Megies, T., Behr, Y., & Wassermann, J. (2010). ObsPy: A python toolbox for seismology. *Seismological Research Letters*, *81*(3), 530–533. https://doi.org/10.1785/gssrl.81.3.530

Bowen, S., Richard, J., Mancini, J., Fessatidis, V., & Crooker, B. (2003). Microseism and infrasound generation by cyclones. *Journal of the Acoustical Society of America*, *113*(5), 2562–2573. https://doi.org/10.1121/1.1567277

Bromirski, P., & Duennebier, F. (2002). The near-coastal microseism spectrum: Spatial and temporal wave climate relationships. *Journal of Geophysical Research*, *107*(B8), 2166–2185. https://doi.org/10.1029/2001JB000265

Bromirski, P., Stephen, R., & Gerstoft, P. (2013). Are deep-ocean-generated surface-wave microseisms observed on land? *Journal of Geophysical Research: Solid Earth*, *118*(B10), 3610–3629. https://doi.org/10.1002/jgrb.50268

Cessaro, R. (1994). Sources of primary and secondary microseisms. *Bulletin of the Seismological Society of America*, *84*(1), 142–148. https://doi.org/10.1785/BSSA0840010142

Cessaro, R., & Chan, W. (1989). Wide-angle triangulation array study of simultaneous primary microseism sources. *Journal of Geophysical Research*, *94*(B11), 15555–15563. https://doi.org/10.1029/JB094iB11p15555

Chen, S., & Curcic, M. (2015). Ocean surface waves in Hurricane Ike (2008) and Superstorm Sandy (2012): Coupled model predictions and observations. *Ocean Modelling*, *103*, 161–176. https://doi.org/10.1016/j.ocemod.2015.08.005

Chen, X., Tian, D., & Wen, L. (2015). Microseismic sources during Hurricane Sandy. *Journal of Geophysical Research: Solid Earth*, *120*(9), 6386–6403. https://doi.org/10.1002/2015JB012282

Chevrot, S., Sylvander, M., Benahmed, S., Ponsolles, C., Lefevre, J., & Paradis, D. (2007). Source locations of secondary microseisms in western Europe: Evidence for both coastal and pelagic sources. *Journal of Geophysical Research*, *112*(B11), B11301. https://doi.org/10.1029/2007JB005059

Chi, W., Chen, W., Kuo, B., & Dolenc, D. (2010). Seismic monitoring of western Pacific typhoons. *Marine Geophysical Researches*, *31*(4), 239–251. https://doi.org/10.1007/s11001-010-9105-x

Davy, C., Barruol, G., Fontaine, F., Sigloch, K., & Stutzmann, E. (2014). Tracking major storms from microseismic and hydroacoustic observations on the seafloor. *Geophysical Research Letters*, *41*(24), 8825–8831. https://doi.org/10.1002/2014GL062319

Ebeling, C. W. (2012). Chapter one—Inferring ocean storm characteristics from ambient seismic noise: A historical perspective. In R. Dmowska (Ed.), *Advances in geophysics* (Vol. 53, pp. 1–33). Elsevier. https://doi.org/10.1016/B978-0-12-380938-4.00001-X

Emanuel, K. (2017a). Assessing the present and future probability of Hurricane Harvey's rainfall. In *Proceedings of the National Academy of Sciences*. https://doi.org/10.1073/pnas.1716222114

Emanuel, K. (2017b). Will global warming make hurricane forecasting more difficult? *Bulletin of the American Meteorological Society*, *98*(3), 495–501. https://doi.org/10.1175/BAMS-D-16-0134.1

Esmersoy, C., Cormier, V., & Toksöz, M. (1985). Three-component array processing (Technical Report). *The VELA Program: A Twenty-five Year Review of Basic Research*.

Esquivel-Trava, B., Ocampo-Torres, F., & Osuna, P. (2015). Spatial structure of directional wave spectra in hurricanes. *Ocean Dynamics*, *65*(1), 55–76. https://doi.org/10.1007/s10236-014-0791-9

Essen, H., Krüger, F., Dahm, T., & Grevemeyer, I. (2003). On the generation of secondary microseisms observed in northern and central Europe. *Journal of Geophysical Research*, *108*(B10), 2506. https://doi.org/10.1029/2002JB002338

Euler, G., Wiens, D., & Nyblade, A. (2014). Evidence for bathymetric control on the distribution of body wave microseism sources from temporary seismic arrays in Africa. *Geophysical Journal International*, *197*(3), 1869–1883. https://doi.org/10.1093/gji/ggu105

Fan, W., McGuire, J., de Groot-Hedlin, C., Hedlin, M., Coats, S., & Fiedler, J. (2019). Stormquakes. *Geophysical Research Letters*, *46*(22), 12909–12918. https://doi.org/10.1029/2019GL084217

Farra, V., Stutzmann, E., Gualtieri, L., Schimmel, M., & Ardhuin, F. (2016). Ray-theoretical modeling of secondary microseism P waves. *Geophysical Journal International*, *206*(3), 1730–1739. https://doi.org/10.1093/gji/ggw242

Friedrich, A., Klinge, K., & Krueger, F. (1998). Ocean-generated microseismic noise located with the Graefenberg array. *Journal of Seismology*, *2*(1), 47–64. https://doi.org/10.1023/A:1009788904007

Fukao, Y., Nishida, K., & Kobayashi, N. (2010). Seafloor topography, ocean infragravity waves, and background Love and Rayleigh waves. *Journal of Geophysical Research*, *115*(B4), B04302. https://doi.org/10.1029/2009JB006678

Gal, M., Reading, A., Ellingsen, S., Koper, K., & Burlacu, R. (2017). Full wavefield decomposition of high-frequency secondary microseisms reveals distinct arrival azimuths for Rayleigh and Love waves. *Journal of Geophysical Research: Solid Earth*, *122*(6), 4660–4675. https://doi.org/10.1002/2017JB014141

GEBCO. (2003). The GEBCO Digital Atlas published by the British Oceanographic Data Centre on behalf of IOC and IHO. Retrieved from https://www.gebco.net/

Gerstoft, P., Fehler, M., & Sabra, K. (2006). When Katrina hit California. *Geophysical Research Letters*, *33*(17), L17308. https://doi.org/10.1029/2006GL027270

Gerstoft, P., Shearer, P., Harmon, N., & Zhang, J. (2008). Global P, PP, and PKP wave microseisms observed from distant storms. *Geophysical Research Letters*, *35*(23), L23306. https://doi.org/10.1029/2008GL036111

Gilmore, M. (1947). Tracking ocean storms with the seismograph. *Bulletin of the American Meteorological Society*, *28*(2), 73–86. https://doi.org/10.1175/1520-0477-28.2.73

Gualtieri, L., Bachmann, E., Simons, F. J., & Tromp, J. (2021). Generation of secondary microseism Love waves: Effects of bathymetry, 3-D structure and source seasonality. *Geophysical Journal International*, *226*(1), 192–219. https://doi.org/10.1093/gji/ggab095

Gualtieri, L., Stutzmann, E., Capdeville, Y., Farra, V., Mangeney, A., & Morelli, A. (2015). On the shaping factors of the secondary microseismic wavefield. *Journal of Geophysical Research: Solid Earth*, *120*(9), 6241–6262. https://doi.org/10.1002/2015JB012157

Guo, Z., Xue, M., Aydin, A., & Ma, Z. (2020). Exploring source regions of single- and double-frequency microseisms recorded in eastern North American margin (ENAM) by cross-correlation. *Geophysical Journal International*, *220*, 1352–1367. https://doi.org/10.1093/gji/ggz470

Gutenberg, B. (1936). On microseisms. *Bulletin of the Seismological Society of America*, *26*(2), 111–117. https://doi.org/10.1785/BSSA0260020111

Gutenberg, B. (1958). In H. Landsberg & J. Mieghem (Eds.), *Microseisms* (Vol. 5, pp. 53–92). Elsevier. https://doi.org/10.1016/S0065-2687(08)60075-8

Hasselmann, K. (1963). On the non-linear energy transfer in a gravity-wave spectrum, Part 2. Conservation theorems; wave particle analogy; irreversibility. *Journal of Fluid Mechanics*, *15*, 273–281. https://doi.org/10.1017/S0022112063000239

Haubrich, R., Munk, W., & Snodgrass, F. (1963). Comparative spectra of microseisms and swells. *Bulletin of the Seismological Society of America*, *53*(1), 27–37. https://doi.org/10.1785/BSSA0530010027

Hello, Y., & Nolet, G. (2020). Floating seismographs (MERMAIDS). In H. K. Gupta (Ed.), *Encyclopedia of Solid Earth Geophysics* (pp. 1–6). Springer International Publishing. https://doi.org/10.1007/978-3-030-10475-7_248-1

Hu, K., & Chen, Q. (2011). Directional spectra of hurricane-generated waves in the Gulf of Mexico. *Geophysical Research Letters*, *38*(19), L19608. https://doi.org/10.1029/2011GL049145

Juretzek, C., & Hadziioannou, C. (2016). Where do ocean microseisms come from? A study of Love-to-Rayleigh wave ratios. *Journal of Geophysical Research: Solid Earth*, *121*(9), 6741–6756. https://doi.org/10.1002/2016JB013017

Juretzek, C., & Hadziioannou, C. (2017). Linking source region and ocean wave parameters with the observed primary microseismic noise. *Geophysical Journal International*, *211*(3), 1640–1654. https://doi.org/10.1093/gji/ggx388

Kedar, S., Longuet-Higgins, M., Webb, F., Graham, N., Clayton, R., & Jones, C. (2008). The origin of deep ocean microseisms in the North Atlantic Ocean. *Proceedings of the Royal Society A: Mathematical, Physical and Engineering Sciences*, *464*(2091), 777–794. https://doi.org/10.1098/rspa.2007.0277

Khan, S., van der Meijde, M., van der Werff, H., & Shafique, M. (2020). The impact of topography on seismic amplification during the 2005 Kashmir earthquake. *Natural Hazards and Earth System Sciences*, *20*(2), 399–411. https://doi.org/10.5194/nhess-20-399-2020

Kibblewhite, A., & Wu, C. (Eds.). (1996). *Wave Interactions as seismo-acoustic source*. Springer. https://doi.org/10.1007/BFb0011210

Knapp, K. R., Applequist, S., Diamond, H. J., Kossin, J. P., Kruk, M., & Schreck, C. (2010). *NCDC International Best Track Archive for Climate Stewardship (IBTrACS) Project, Version 3. [2010–2019 catalogue]*. NOAA National Centers for Environmental Information. https://doi.org/10.7289/V5NK3BZP

Knapp, K. R., Kruk, M., Levinson, D., Diamond, H., & Neumann, C. (2010). The International Best Track Archive for Climate Stewardship (IBTrACS): Unifying tropical cyclone best track data. *Bulletin of the American Meteorological Society*, *91*(3), 363–376. https://doi.org/10.1175/2009BAMS2755.1

Knauss, J. (1997). *Introduction to physical oceanography* (2nd ed.). Waveland Press, Inc.

Kossin, J., Emanuel, K., & Vecchi, G. (2014). The poleward migration of the location of tropical cyclone maximum intensity. *Nature*, *509*(7500), 349–356. https://doi.org/10.1038/nature13278

Kossin, J., Knapp, K., Olander, T., & Velden, C. (2020). Global increase in major tropical cyclone exceedance probability over the past four decades. *Proceedings of the National Academy of Sciences*, *117*(22), 11975–11980. https://doi.org/10.1073/pnas.1920849117

Landès, M., Hubans, F., Shapiro, N., Paul, A., & Campillo, M. (2010). Origin of deep ocean microseisms by using teleseismic body waves. *Journal of Geophysical Research*, *115*(B5), B05302. https://doi.org/10.1029/2009JB006918

Le Pape, F., Craig, D., & Bean, C. J. (2021). How deep ocean-land coupling controls the generation of secondary microseism Love waves. *Nature Communications*, *12*(2332), 2562–2573. https://doi.org/10.1121/1.1567277

Lin, J., Lin, J., & Xu, M. (2017). Microseisms generated by super typhoon Megi in the western Pacific Ocean. *Journal of Geophysical Research: Oceans*, *122*, 1–12. https://doi.org/10.1002/2017JC013310

Löer, K., Riahi, N., & Saenger, E. H. (2018). Three-component ambient noise beamforming in the Parkfield area. *Geophysical Journal International*, *213*(3), 1478–1491. https://doi.org/10.1093/gji/ggy058

Longuet-Higgins, M. (1950). A theory of the origin of microseisms. *Philosophical Transactions of the Royal Society of London. Series A, Mathematical and Physical Sciences*, *243*, 1–35. https://doi.org/10.1098/rsta.1950.0012

Longuet-Higgins, M. (1953). Can sea waves cause microseisms? In N. R. Council (Ed.), *Symposium on microseisms: Held at Arden House, Harriman, NY 4–6 September 1952, Sponsored by the Office of Naval Research, and the Geophysical Research Directorate of the U.S. Air Force*. The National Academies Press. https://doi.org/10.17226/18689

Matsuzawa, T., Obara, K., Maeda, T., Asano, Y., & Saito, T. (2012). Love- and Rayleigh-wave microseisms excited by migrating ocean swells in the North Atlantic detected in Japan and Germany. *Bulletin of the Seismological Society of America*, *102*(4), 1864–1871. https://doi.org/10.1785/0120110269

Nakata, N., Gualtieri, L., & Fichtner, A. (Eds.). (2019). *Seismic ambient noise*. Cambridge University Press. https://doi.org/10.1017/9781108264808

Natural Resources Canada (NRCAN Canada). (1975). *Canadian National Seismograph Network*. International Federation of Digital Seismograph Networks. Retrieved from https://www.fdsn.org/networks/detail/CN/

Nishida, K. (2017). Ambient seismic wave field. *Proceedings of the Japan Academy, Series B*, *93*(7), 423–448. https://doi.org/10.2183/pjab.93.026

Nishida, K., Kawakatsu, H., Fukao, Y., & Obara, K. (2008). Background Love and Rayleigh waves simultaneously generated at the Pacific Ocean floors. *Geophysical Research Letters*, *35*(16), L16307. https://doi.org/10.1029/2008GL034753

Ochi, M. (2003). *Hurricane-generated seas* (1st ed.). Elsevier.

Park, S., & Hong, T. (2020). Typhoon-induced microseisms around the South China Sea. *Seismological Research Letters*, *91*(6), 3454–3468. https://doi.org/10.1785/0220190310

Retailleau, L., & Gualtieri, L. (2021). Multi-phase seismic source imprint of tropical cyclones. *Nature Communications*, *12*(1), 2064. https://doi.org/10.1038/s41467-021-22231-y

Rodgers, A., Petersson, N., & Sjogreen, B. (2010). Simulation of topographic effects on seismic waves from shallow explosions near the North Korean nuclear test site with emphasis on shear wave generation. *Journal of Geophysical Research*, *115*(B11), B11309. https://doi.org/10.1029/2010JB007707

Saito, T. (2010). Love-wave excitation due to the interaction between a propagating ocean wave and the sea-bottom topography. *Geophysical Journal International*, *182*(3), 1515–1523. https://doi.org/10.1111/j.1365-246X.2010.04695.x

Sepúlveda, S., Murphy, W., Jibson, R., & Petley, D. (2005). Seismically induced rock slope failures resulting from topographic amplification of strong ground motions: The case of Pacoima Canyon, California. *Engineering Geology*, *80*(3–4), 336–348. https://doi.org/10.1016/j.enggeo.2005.07.004

Stutzmann, E., Ardhuin, F., Schimmel, M., Mangeney, A., & Patau, G. (2012). Modelling long-term seismic noise in various environments. *Geophysical Journal International*, *191*(2), 707–722. https://doi.org/10.1111/j.1365-246X.2012.05638.x

Sufri, O., Koper, K. D., Burlacu, R., & de Foy, B. (2014). Microseisms from superstorm Sandy. *Earth and Planetary Science Letters*, *402*, 324–336. https://doi.org/10.1016/j.epsl.2013.10.015

Sutton, G., & Barstow, N. (1996). Ocean bottom microseisms from a distant super typhoon. *Geophysical Research Letters*, *23*(5), 499–502. https://doi.org/10.1029/96GL00419

Tabulevich, V. (1971). The effect of the velocity of the centre of a cyclone on the generation of microseisms. *Pure and Applied Geophysics*, *85*(1), 69–74. https://doi.org/10.1007/BF00875399

Tanimoto, T. (2013). Excitation of microseisms: Views from the normal-mode approach. *Geophysical Journal International*, *194*(3), 1755–1759. https://doi.org/10.1093/gji/ggt185

Tanimoto, T., Hadziioannou, C., Igel, H., Wassermann, J., Schreiber, U., Gebauer, A., & Chow, B. (2016). Seasonal variations in the Rayleigh-to-Love wave ratio in the secondary microseism from colocated ring laser and seismograph. *Journal of Geophysical Research: Solid Earth*, *121*(4), 2447–2459. https://doi.org/10.1002/2016JB012885

Tanimoto, T., & Rivera, L. (2005). Prograde Rayleigh wave particle motion. *Geophysical Journal International*, *162*(2), 399–405. https://doi.org/10.1111/j.1365-246X.2005.02481.x

Tanimoto, T., & Valovcin, A. (2015). Stochastic excitation of seismic waves by a hurricane. *Journal of Geophysical Research: Solid Earth*, *120*(11), 7713–7728. https://doi.org/10.1002/2015JB012177

Tolman, H., Accensi, M., Alves, J.-H., Ardhuin, F., Bidlot, J., Booij, N., et al. (2014). User manual and system documentation of WAVEWATCH III version 4.18. *Technical Note*.

Traer, T., Gerstoft, P., Bromirski, P., & Shearer, P. (2012). Microseisms and hum from ocean surface gravity waves. *Journal of Geophysical Research*, *117*(B11), B11307. https://doi.org/10.1029/2012JB009550

Wallace, J., & Hobbs, P. (2006). *Atmospheric science—An introductory survey* (2nd ed.). Elsevier.

Wang, Z., Niu, F., Huang, J., Li, Z., & Chen, H. (2021). Distribution of Rayleigh wave microseisms constrained by multiple seismic arrays. *Journal of Geophysical Research: Solid Earth*, *126*(9), e2021JB022084. https://doi.org/10.1029/2021JB022084

Ward Neale, J., Harmon, N., & Srokosz, M. (2018). Improving microseismic P wave source location with multiple seismic arrays. *Journal of Geophysical Research: Solid Earth*, *123*(1), 476–492. https://doi.org/10.1002/2017JB015015

Ying, Y., Bean, C., & Bromirski, P. (2014). Propagation of microseisms from the deep ocean to land. *Geophysical Research Letters*, *41*(18), 6374–6379. https://doi.org/10.1002/2014GL060979

Young, I. (1998). Observations of the spectra of hurricane generated waves. *Ocean Engineering*, *25*(4–5), 261–276. https://doi.org/10.1016/S0029-8018(97)00011-5

Young, I. (2006). Directional spectra of hurricane wind waves. *Journal of Geophysical Research*, *111*(C8), C08020. https://doi.org/10.1029/2006JC003540

Zhang, J., Gerstoft, P., & Bromirski, P. (2010). Pelagic and coastal sources of P-wave microseisms: Generation under tropical cyclones. *Geophysical Research Letters*, *37*(15), L15301. https://doi.org/10.1029/2010GL044288

Ziane, D., & Hadziioannou, C. (2019). The contribution of multiple scattering to Love wave generation in the secondary microseism. *Geophysical Journal International*, *217*(2), 1108–1122. https://doi.org/10.1093/gji/ggz056